

Solar magnetic fluxtubes diagnosed from isolated
internetwork bright points - An analysis of Dutch
Open Telescope observations

E.M.W.P. Haverkamp

2004-08-30

Contents

1	Introduction	4
2	The Dutch Open Telescope	7
2.1	Introduction	7
2.2	Tower, telescope and canopy	8
2.3	Multi-wavelength re-imaging	8
2.4	Speckle acquisition and reconstruction	11
3	Data reduction Ca II H	11
3.1	Network, intermediate and internetwork regions	11
3.2	Convolution of Ca II H data	13
3.3	Time-averaging and removal of background	15
3.4	Binary map of Ca II H data	15
3.4.1	Erosion-dilation processing	15
3.4.2	Removing more noise	17
3.5	Identifying BPs	21
4	Data reduction G band	21
4.1	Convolution of G band data	21
4.2	Time-averaging and removal of background	21
4.3	Dilation of binary map Ca II H BPs	21
4.4	Binary map of G-band data	22
4.5	Removing noise and identifying BPs	23
5	Analysis of Ca II H BPs	24
5.1	Lifetime	24
5.2	Average diameter	24
5.3	Average velocity	29
5.4	Possible relations ?	29
5.5	Intensity profiles and wavelet analysis	30
6	Analysis of G-band BPs	30
6.1	Lifetime	30
6.2	Average diameter	30
6.3	Average velocity	35
6.4	Possible relations ?	35
6.5	Intensity profiles and wavelet analysis	35
7	Cospatial and cotemporal BPs	37
8	Discussion	40
9	Conclusion	41
A	The theory of convective collapse of magnetic fluxtubes	45

1 Introduction

The solar atmosphere consists of several layers that are different in many aspects. The surface that we see when we observe the sun, is the region where the sun loses most of its energy through radiation. The energy that is generated in the core of the sun through nuclear fusion is transported through the interior of the sun to the outer layers until the gas becomes dense enough for photons to escape into space. Below the surface the sun transports its energy by convection, which means that energy transport takes place by transporting hot and cold bubbles of gas up and down (towards and away from the surface). When these bubbles arrive near the surface they lose much energy through radiation. The temperature of the bubble decreases and causes the gas to sink back into the sun. The resulting surface pattern is called granulation and can clearly be seen with telescopes. The temperature of the gas is around 5700 K at the surface. The gas pressure determines the topography there.

Above the surface the temperature and pressure decrease through the photosphere up to the chromosphere, where the gas pressure still drops but the temperature rises again towards the corona which has temperatures of $1 - 2 \times 10^6$ K. Magnetic energy that rises through the atmosphere determines the topography here and must be responsible in one way or another for the dramatic temperature increase.

Isolated small-scale magnetic field concentrations in the internetwork photosphere and chromosphere of the sun are the subject of this research. These magnetic fluxtubes are the basic building blocks of solar magnetism. They appear everywhere where there is magnetic activity. They are observed near sunspots, at plage, in the network and even in the internetwork where the fluxtubes are sparse and isolated and therefore good to measure.

There are much open questions regarding solar magnetic fluxtubes. Questions about their patterning, i.e. how is their distribution over the solar surface? How are they produced? By a global or local dynamo? The time scale on which they live raises questions (granular or longer). And how are these fluxtubes connected? Are the fluxtubes closed or open to the corona? Finally, the dynamics of the fluxtubes raises questions regarding foot-point forcing and wave modes.

In this research, we used dual-wavelength observations from the Dutch Open Telescope (DOT, Rutten et al. 2003) to measure properties of solar magnetic fluxtubes observed as bright points. We accomplish this by finding isolated bright points in the internetwork chromosphere and measuring them in the photosphere. Bright points (BPs) are identified with small magnetic concentrations and were first reported by Dunn & Zirker (1973) for the photosphere and by Mehlretter (1974) for the chromosphere.

We have used cospatial and cotermporal G-band and Ca II H imaging to find BPs in the solar photosphere and chromosphere, respectively. The data were produced on 2003-05-02 at 10:35-11:16 UT. An area of 73×58 arcsec² was imaged during 41 minutes. The resulting sequence consists of 154 speckle-restored images taken synchronously at 16 s cadence using four different interference filters. In addition to the Ca II H and G-band filters, the area was also imaged using filters for the blue and red continuum (Fig. 1).

Whenever there is magnetic activity in the solar photosphere, BPs appear in intergranular lanes. They even occur in the internetwork areas of the quiet-sun surface outside active regions (Fig. 2). The internetwork area is a region where

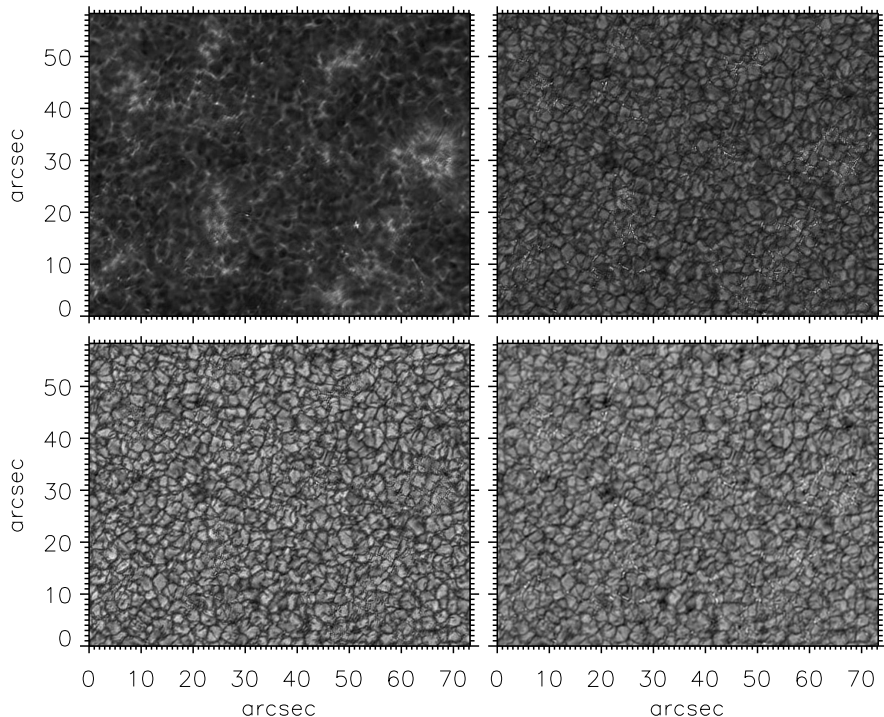


Figure 1: cospatial and cotermporal Dutch Open Telescope observations produced on 2003-05-02 at 10:35-11:16 UT. The whole field of view is $73 \times 58 \text{ arcsec}^2$ and shows a quiet area of the solar surface without active regions. The sequence consists of 154 speckle-restored images taken synchronously at 16s cadence and therefore has a time-span of 41 minutes. From top to bottom, left to right: Ca II H, G band, blue continuum and red continuum

there is little magnetic activity, compared to network areas which are dominated by magnetic activity. BPs are regarded as magnetic elements (Berger et al. 1996, Sanchez Almeida, 2001) that extend from the convection zone up into the chromosphere and are clearly visible in G-band and Ca II H observations. Previous observations (Berger et al. 1996, Sütterlin 2001, Langhans 2003) have shown that BPs are small sub-arcsecond elements and that they have a short dynamic lifetime (time scale of granular dynamics). Merging and splitting of BPs occurs all the time; we will show some examples in this report. The connection of BPs to magnetic elements is well accepted, but the process that causes the brightening of the elements is still under debate. Spruit (1977) pioneered the theory of convective collapse of magnetic elements in the solar atmosphere. This collapse can cause the elements to become bright especially when imaged in the G band.

Extensive data-reduction on the Ca II H data enabled us to get a good sample of BPs to use in our analysis. We find 188 BPs with the Ca II H filter and 134 BPs in the corresponding areas in the G band. Our results show lifetimes, velocities and sizes of the BPs and a possible relation between them. We pro-

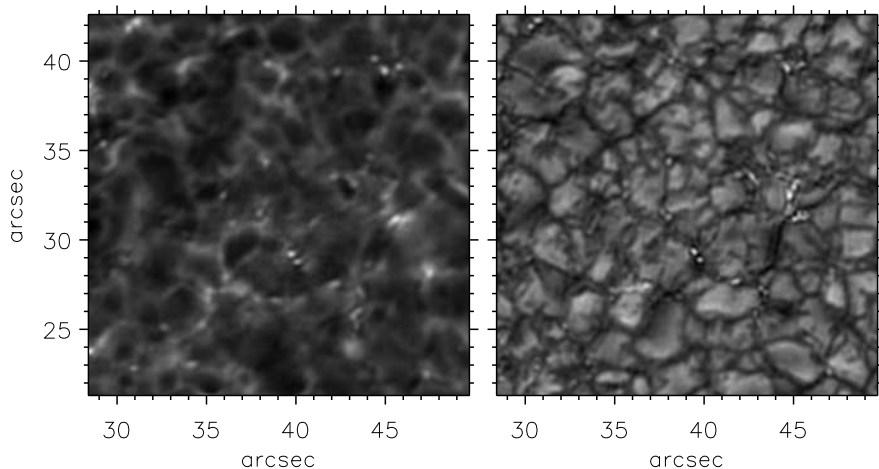


Figure 2: center part of the field of view imaged on 2003-05-02 showing BPs in chromosphere and photosphere. Left: Ca II H data which images the chromosphere. Right: G-band data showing the photosphere with granulation. Notice the BPs just below the center of the data in the dark lane between the granules. The images show a small region in the center of the imaged field and is $21 \times 21 \text{ arcsec}^2$. The axis correspond to the axis of Fig. 1.

duced intensity profiles in both wavelengths and performed wavelet analysis on these to see whether there are significant periodicities in the BP brightness. Finally, we show the reader some examples of cospatial and cotemporal BPs which suggest that intermittent BPs can sometimes signify the presence of longer-lived patches of magnetic field.

We have exploited the capability of the Dutch Open Telescope to observe simultaneously and cospatially in the G band and in Ca II H to search for cotemporal and cospatial BPs in the photosphere and chromosphere, respectively. Other research (Berger 1996, Sanchez Almeida, J. 2001, Sanchez Almeida, J. et al. 2004, Nisenson, P. et al. 2003, van Ballegoijen & A. A. and Nisenson, P., 2002) only focused on photospheric BPs. In this report, we will show that BPs are larger, have longer lifetimes on average and move faster in the chromosphere when compared to the photosphere. BPs are much harder to find in the G band than in Ca II H, because their sizes in the photosphere are often smaller than the angular resolution limit of the telescope which is 0.2 arcsec for the Dutch Open Telescope. The angular resolution limit corresponds to a distance on the sun of roughly 145 km. The contrast of the chromospheric BPs is much better in the Ca II H data when compared to the photospheric BPs in the G-band data. We therefore started our BP search in the Ca II H observations. From the cospatial and cotemporal observations we were able to identify corresponding BPs in both wavelengths. The BPs that we find in the internetwork chromosphere show a very patchy distribution over the internetwork. These patches persist during the whole observation in both chromosphere and photosphere, indicating mesogranular time scales. The BPs in these patches individually show granular time scales, but as a group they indicate much longer field patch lifetimes.



Figure 3: Dutch Open Telescope on La Palma.

2 The Dutch Open Telescope

2.1 Introduction

The Dutch Open Telescope (DOT) is an innovative optical solar telescope at the Roque de los Muchachos Observatory on La Palma (Canary Islands).

The DOT was designed and built by R.H. Hammerschlag of the Sterrenkundig Instituut Utrecht with a small team of coworkers at IGF Utrecht and DTO Delft. We give a short description following Rutten et al. (2004a).

The innovative open design of the DOT is well seen in Fig. 3. The Roque de los Muchachos observatory site is well-known to deliver extraordinary seeing quality and is therefore exploited in nighttime astronomy as well as in solar observing. Around the island is a low inversion layer that often keeps the clouds below the volcano rim. The strong trade winds keep the local turbulent convection from solar ground heating to a small layer below the 15 m high open-tower top and they blow through the telescope, flushing the 45 cm primary mirror and keeping the telescope safe from internal turbulence. The DOT is a high-resolution tomographer, providing multi-wavelength image and Doppler-gram sequences that sample the photosphere and chromosphere. The sequences have high angular resolution nearing the diffraction limit of 0.2 arcsec already at fair seeing with a cadence about 20s over rather large fields ($90 \times 60 \text{ arcsec}^2$) and durations (possibly up to eight hours).

designation	$\lambda(\text{\AA})$	width(\AA)	type	tuning
blue continuum	4320	6	interference	fixed
red continuum	6540	3	interference	tiltable
G Band	4305	10	interference	fixed
Ca II H	3968	1.35	interference	tiltable
H α	6563	0.25	Lyot	tunable
Ba II	4554	0.08	Lyot	tunable

Table 1: DOT filter specification.

2.2 Tower, telescope and canopy

The principals behind the DOT design and construction were to achieve high pointing stability and considerable wind buffeting. The foundation of the tower consists of four 2m deep blocks of 25 m³ concrete each. The tower is 15 m high and open and consists of four isosceles triangles of 24.5 cm diameter steel tubes that support an open-mesh telescope platform which is stiffened by a downward framework. The telescope mount is a massive parallactic fork resting on three of the four tower-triangle tops and is extremely rigid.

The primary mirror of the telescope is parabolic with a diameter of $D = 450$ mm and a focal length $f = 200$ cm (Fig. 4). It is made of aluminized Cervit with a protective quartz coating. It is mounted with 3 radial supports of its central hole and 9 cantilevered supports distributed over its backside that exert non-radial forces only. The top contains the primary-focus field stop, re-imaging and multi-wavelength optics, narrow-band filters and the CCD cameras. All supported by heavy steel tubes in triangular geometry similar to the tower with large stiffness against translational perturbations.

The telescope is protected against weather by a 7 m diameter fold-away clamshell canopy, made of heavy PVC cloth supported by heavy steel ribs. It is designed to be closeable in winds up to 30 m/s and to withstand hurricanes up to 70 m/s.

More details on DOT design and hardware is given in Bettonvil et al. (2003).

2.3 Multi-wavelength re-imaging

The system is summarized systematically in Fig. 4. Six channels feed six identical CCD cameras with cospatial images through different filters all specified in Table 1. Each filter has its own diagnostic value, respectively,

- G Band: small part of the solar spectrum with much absorption lines of the CH-molecule, which makes it a dark feature in the spectrum and was labeled G by Fraunhofer who classified strong absorption lines in the solar spectrum (Fig. 5). It brightens considerably in magnetic elements, probably due to enhanced hot-wall visibility from molecular dissociation. (e.g. Rutten et al. 2001B; Langhans et al. 2002). It is the preferred diagnostic to locate and follow small intergranular elements (e.g. Title & Berger 1996; Berger et al. 1998a, 1998b).
- Ca II H: mapping of chromospheric network and internetwork oscillation patterns (Lites et al. 1999). Ca II H absorption line visible in Fig. 5.

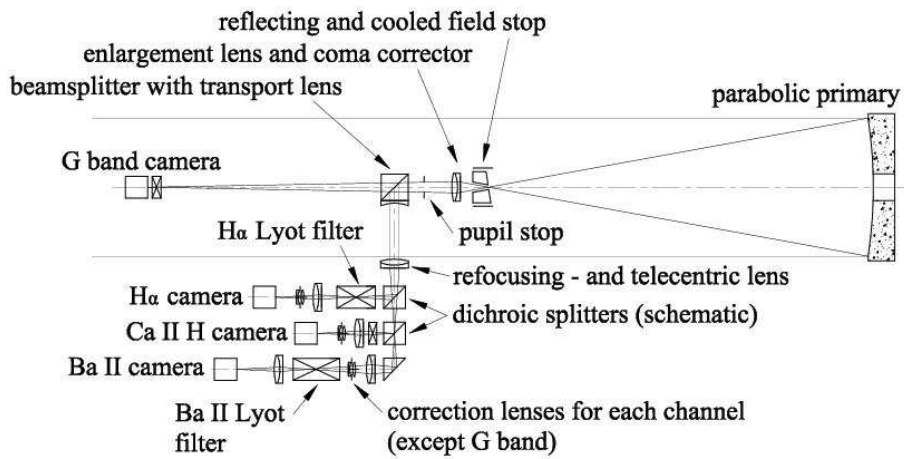
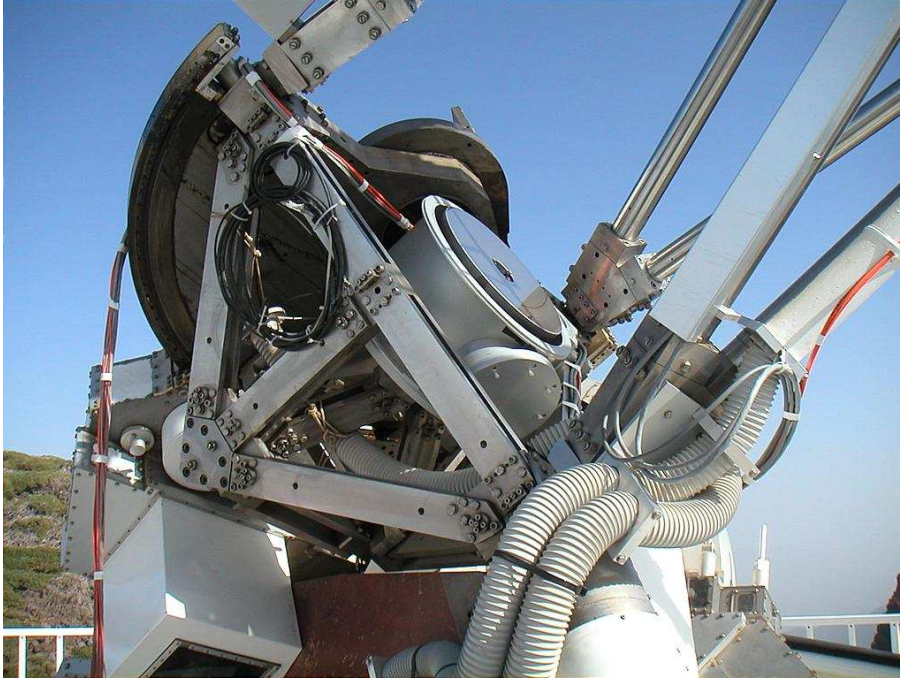


Figure 4: top: Mount and mirror of the Dutch Open Telescope. Bottom: Sketch of the DOT multi-wavelength re-imaging optics. The Blue and Red continua channels are omitted. The actual 3-dimensional configuration differs considerably. See Bettonvil et al. (2003) for details.

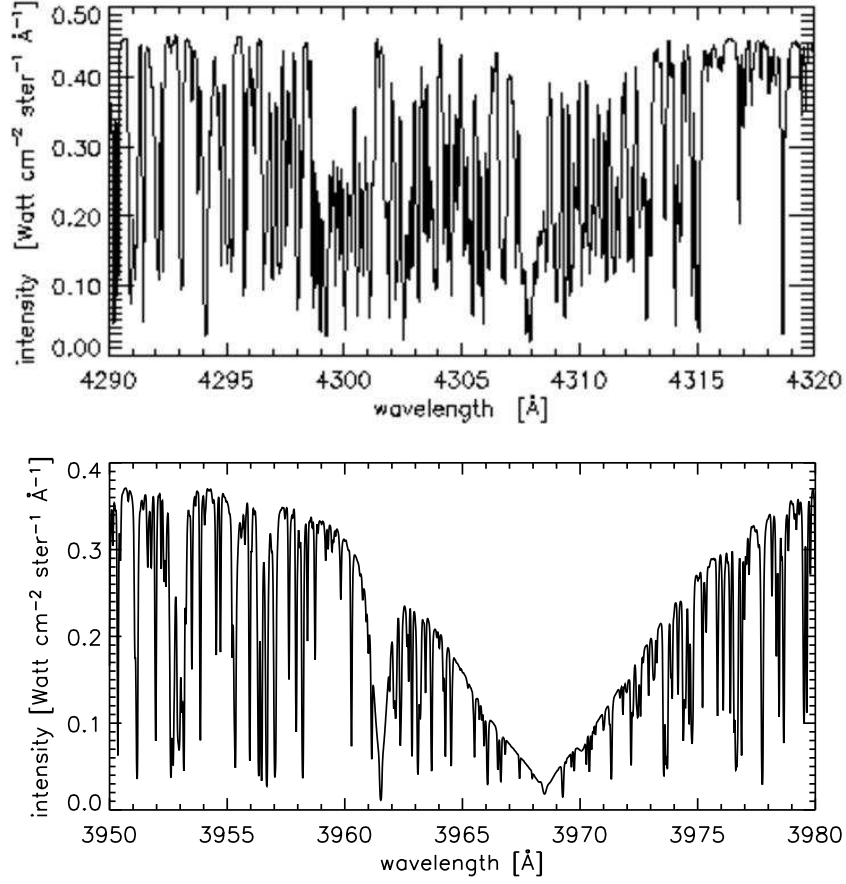


Figure 5: short segments of the solar spectrum. Top: the G band classified by Fraunhofer with G containing many absorption lines of the CH molecule. Bottom: Ca II H absorption line. Ca II H and K are the strongest lines in the visible solar spectrum.

- Blue continuum: useful to disentangle granulation and magnetic BPs through differentiation with synchronous G-band images (van Ballegoijen et al. 1998).
- Red continuum: primarily added to enable dual-channel H α restoration, but of interest in itself as longer-wavelength sample of the low photosphere.
- H α : mapping of low-lying loops complementary to EUV coronal loops as well as the foot-points of hot X-ray loops (e.g. Schrijver & Title 2002).
- Ba II: a very promising mid-photosphere Doppler diagnostic due to its wide but boxy profile shape and large atomic mass (Sütterlin et al. 2001b).

2.4 Speckle acquisition and reconstruction

The DOT uses Hitachi KP-F100 cameras with Sony ICX085 CCD chips, 1296×1030 pixel² and pixel size $6.7 \mu\text{m}$. The angular resolution element is 0.071 arcsec/pixel and limits the field to 92×73 arcsec². Each camera is connected through a dual 400-Mbps 100-m long optical fiber link to its own data-acquisition computer. About 100 frames with exposures below 10 ms (speckle bursts) are written to disk and then taped for off-line speckle reconstruction. Extensive pre-processing encompasses dark subtraction and flat-field scaling, co-alignment of all the frames per burst and field tessellation into isoplanatic subfields. The speckle reconstruction code corrects for the asymmetrical DOT aperture obstruction and for camera non-linearity. Subsequent post-processing consists of subfield matching to the mean of the speckle burst, subfield re-assembly into a full reconstructed image, image-to-image alignment to generate a movie per wavelength and movie to movie co-alignment between wavelengths.

3 Data reduction Ca II H

We start our BP search in the chromosphere where the BPs are easier to find. To find as much BPs as we can we have written routines that help us in locating the BPs, instead of visual selection from the data. This chapter explains the whole process of data reduction of the Ca II H data, from the original data to a set of BPs that can be analyzed.

3.1 Network, intermediate and internetwork regions

When there is magnetic activity there are BPs, but there are regions that differ quite drastically in how much activity there actually is. The best place to find individual BPs is the internetwork area where there is little activity. To start with our data-reduction, we need to define these regions in our dataset.

Our data shows regions with much magnetic activity during the whole time sequence of the dataset and are called network (NW), which are not suitable for our investigation. BPs are merging and splitting all the time, which makes it very difficult to do a correct analysis of the BPs in these regions. The NW is clearly visible in the Ca II H data as the white areas.

The regions between and around the network where there is little magnetic activity is called the internetwork (IN). Between internetwork and network is a transition region where there are magnetic elements moving from or to the network and the activity varies in time. This we call the intermediate (IM) zone.

We define our regions using masks for each region that are defined for the whole time series. The IN mask will be the most important one, because this region stays very quiet during the whole time series showing only a couple of magnetic elements that we can track individually.

To define our regions we produced an image of the Ca II H data averaged over the whole time series (Fig. 6). We then made a histogram of the brightness per pixel in this image. All pixels that have intensities below the peak value of 909 are designated as internetwork (IN). Pixels with brightness above 1300 are categorized as network (NW) and pixels between these two boundaries make up

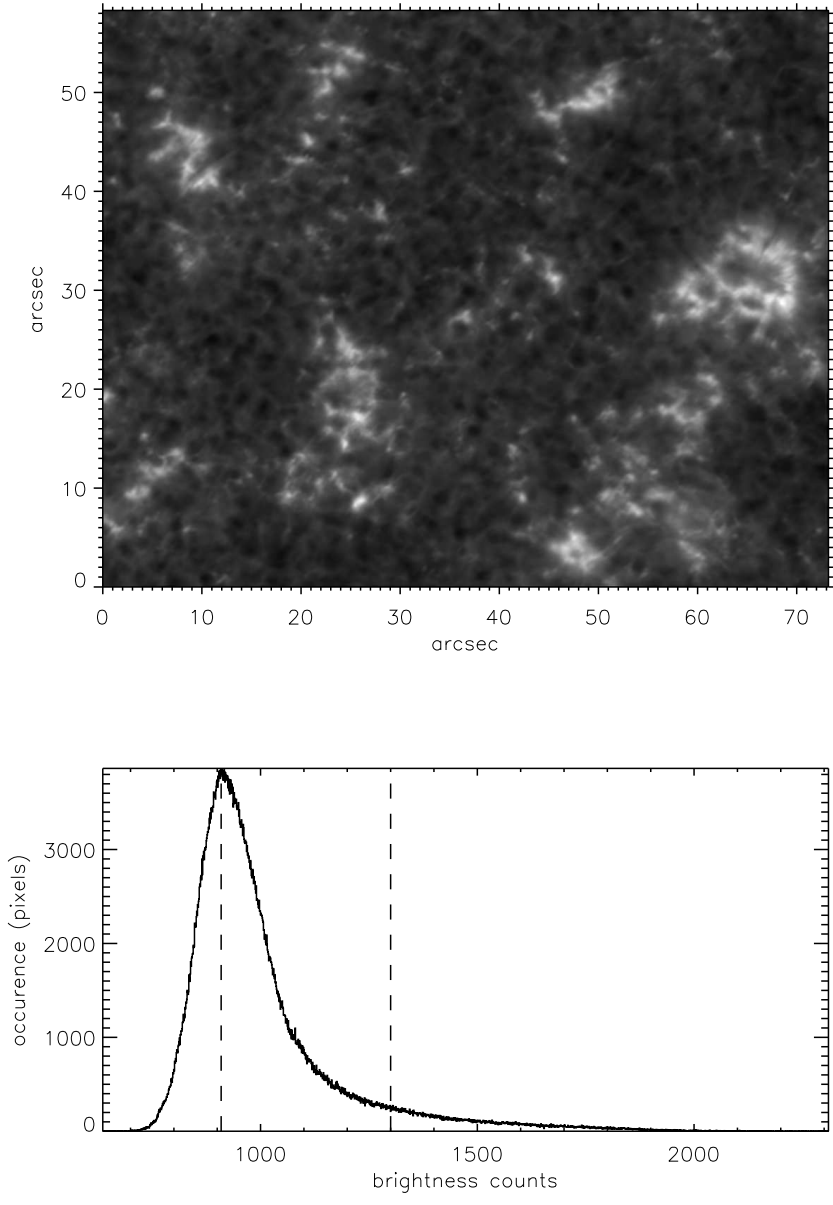


Figure 6: top: Ca II H averaged over the whole duration of the observation. Bottom: histogram of brightness counts in Ca II H averaged image. The two vertical dashed lines indicate the boundary values for the different regions in the data. All pixels to the left of the peak value of 909 brightness counts are designated as internetwork (IN). Pixels with brightness above 1300 are network (NW) and pixels with brightness between these two boundaries form the intermediate (IM) zone.

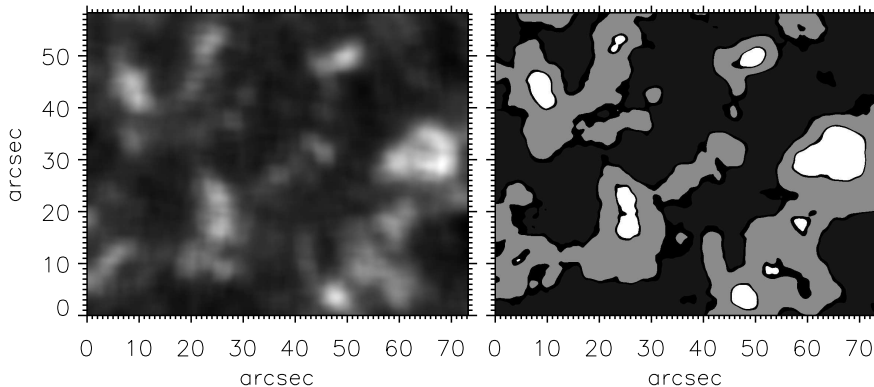


Figure 7: left: This is the Ca II H time-averaged image after smoothing it over 50 pixels. Right: This image shows the masking for the different regions. White is network (NW), gray is intermediate (IM) and dark gray is internetwork (IN). The black lines in between are gaps between the boundaries

the intermediate (IM) zone. We chose to leave small gaps between these boundaries, so some pixels do not belong to any region. We performed a smoothing operation on this time-averaged Ca II H image and applied the boundaries given by the histogram on this image to obtain suitable masks for the different regions. Fig. 7 shows the time-averaged Ca II H image where each pixel is smoothed with the surrounding 50 pixels and the final masks that defines our regions for NW, IM and most importantly the IN.

3.2 Convolution of Ca II H data

To find the BPs for our investigation we developed several programs to help us track down these magnetic fluxtubes and follow them in time. We wrote a feature-finding routine to enhance the BPs in the data and to smooth out features that are different in shape and time scale.

Visual inspection of the data made clear that BPs most of the time have a circular peak-like structure and exist for more than 150s. The first step was to do a convolution of a kernel, which represents a bright point, with the whole Ca II H dataset that was Fourier filtered with a low-pass filter to remove features that change must faster than our magnetic elements. The kernel is 7×7 pixel² in size, which corresponds to 0.5×0.5 arcsec² on the solar surface (Fig. 8). The shape of the kernel is symmetric around its center and both x and y components are given by

$$Z_x = 1 + \sin x \quad (1)$$

and

$$Z_y = 1 + \sin y \quad (2)$$

The range of the x and y coordinates is $[0, \pi]$ and the $x - y$ kernel Z_{xy} is produced by

$$Z_{xy} = (Z_x \times Z_y)^3 \quad (3)$$

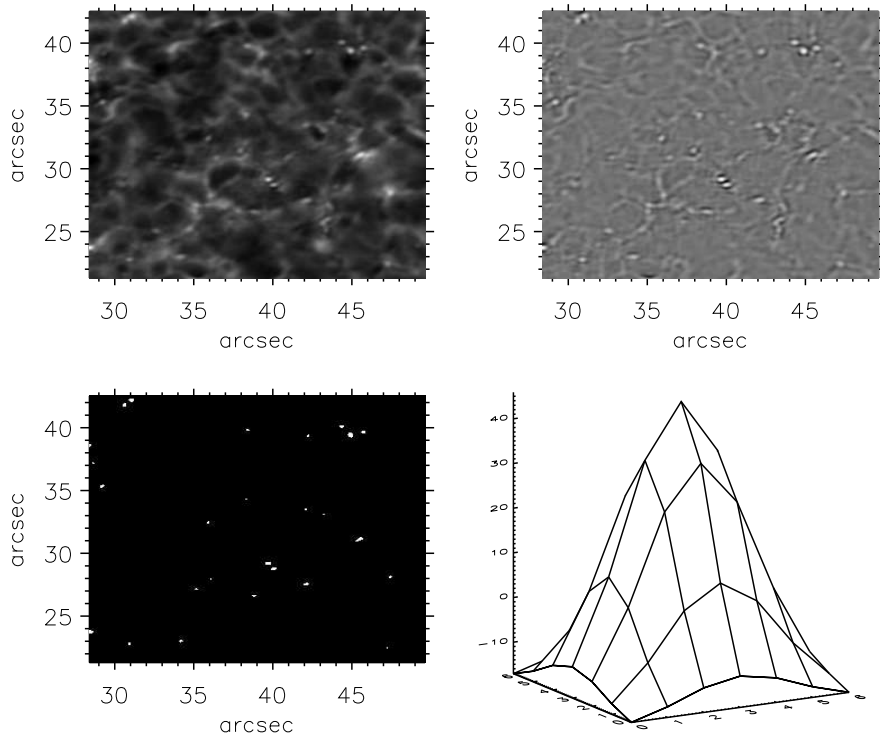


Figure 8: top left: same Ca II H image as in Fig. 2. Top right: Ca II H image after performing the convolution with the kernel which is shown bottom right. Bottom left: Ca II H image after convolution, time-averaging with previous and next images and after removing the gray background. Bottom right: kernel Z_{xy} that we have used to perform a convolution with the original data to search for BPs. The kernel is $7 \times 7 \text{ pixel}^2$ and has the form of the intensity distribution of an imaginary BP. The effect is that structures in the data that are similar to the shape of the kernel are enhanced, whereas other structures will be smoothed out.

Finally, the average value of Z_{xy} is subtracted from Z_{xy} to give a kernel with an average value of zero. This ensures that when the kernel moves over a structure of roughly that shape it enhances it. Other structures are smoothed out.

Convolution of data $f(x)$ with a function $g(x)$ is defined as

$$f * g(x) = \int_{-\infty}^{\infty} f(x') \cdot g(x - x') dx'. \quad (4)$$

This can be extended in more dimensions. We did a 2D convolution on the data, only in the $x - y$ directions of the data (not in the time direction). The kernel moves over the the entire dataset, image for image and at each pixel where the kernel is centered it is multiplied with the data on which the kernel is, producing a new $7 \times 7 \text{ pixel}^2$ area which then is integrated to give to the original pixel a new value.

The kernel proved to be very efficient in enhancing the BPs and removing other signals. Fig. 8 shows the same region of the Ca II H data as in Fig. 2. You

can clearly see that circular structures are enhanced, whereas other structures are smoothed out.

3.3 Time-averaging and removal of background

In addition to the BPs in the Ca II H data, there are more features present that need our attention. Reversed granulation (Rutten et al. 2003) is seen clearly. These arc-shaped structures move quite fast and rarely become as bright as the BPs. There are also acoustic shocks in the data which are short-lived, but repeat themselves in about roughly 3 minute intervals. The reversed granulation and acoustic shocks can be partly removed by averaging the data in time. For each image in the data we took the average of that image with the previous and next image. This way, structures that move fast are also smoothed out.

The convolution of our kernel with the data did produce a gray background, which can be seen in Fig. 8. By removing this background we increase the contrast in our data. We used a routine that scales each image in the sequence, by putting the maximum at the lowest local maximum and the minimum at the highest local minimum in the image. Taking the average value of the data in each image for the minimum, everything below the average is removed and maxima in the data show up with higher contrast. This is clearly shown in Fig. 8 and 9.

3.4 Binary map of Ca II H data

After masking the data with our internetwork mask, we isolated the BPs by thresholding the data at a certain level.

Everything below the threshold value is assigned a 0, everything above becomes a 1, thus producing a binary map of our data. The threshold value must be taken carefully. Taking it too low introduces too much noise (structures that are not BPs), whereas if we take it too high, we might throw away some BPs.

We do however need to take it quite low to keep the BPs connected in time because they can become very weak during their lifetime. The resulting binary map therefore remains noisy. One of the solutions to counter this is to perform erosion-dilation processing.

3.4.1 Erosion-dilation processing

We perform erosion-dilation processing on the data with two different kernels. A kernel that works in the $x - y$ directions, to remove small structures and to enhance structures that are larger than the kernel. The other kernel works in the time direction. It removes short-lived elements and enhances the elements that live longer. Care must be taken that the kernels do not become too large, because in that case different BPs will overlap and will be identified as the same BP. After careful examination we used the following kernels.

The first kernel is a 2D array of 3×3 elements $(x,y) : K1 =$

$$\begin{matrix} & 1 & 1 & 1 \\ 1 & 1 & 1 & \\ & 1 & 1 & 1 \end{matrix}$$

The second kernel is a 3D array of $1 \times 1 \times 3$ elements $(x,y,t) : K2 =$

$$\begin{matrix} & & & 1 \\ & & & 1 \\ & & & 1 \end{matrix}$$

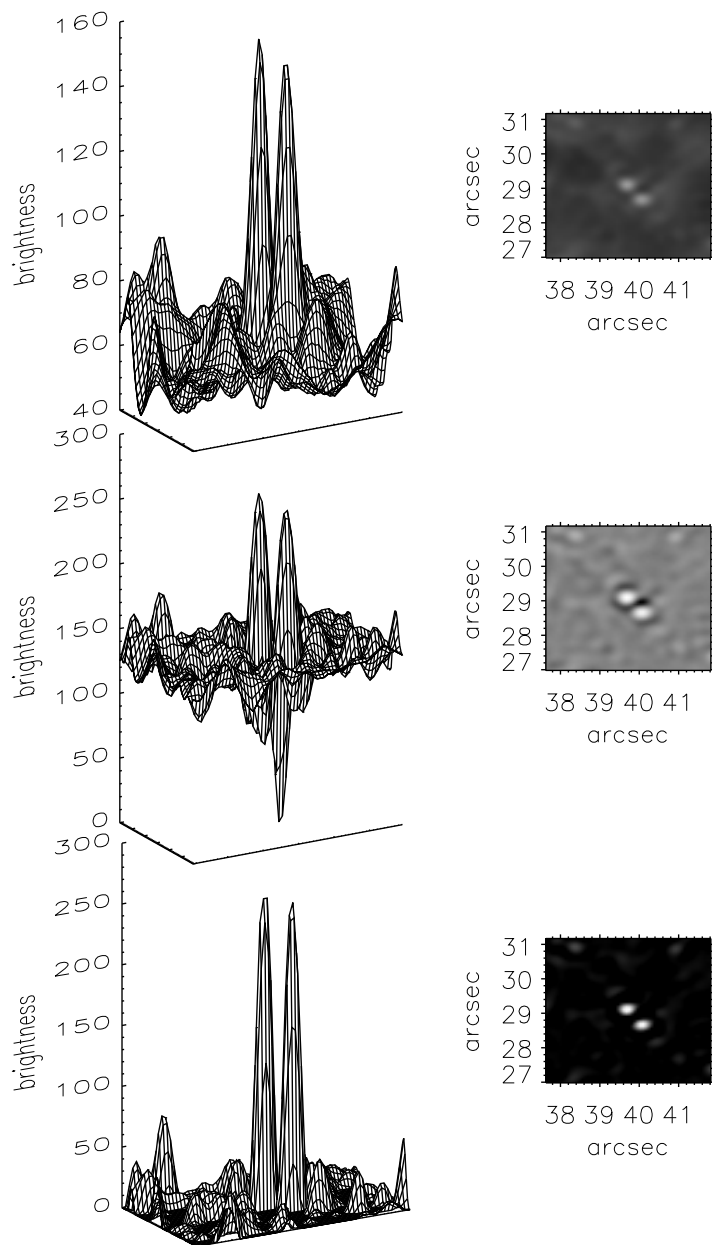


Figure 9: 3 intensity plots and 3 images of the BPs in the center of Fig. 2. Top: original Ca I H data. Middle: convoluted data. Bottom: convoluted, time-averaged and background-removed data. The intensity of the three intensity plots are scaled to byte type to show what happens with the data.

Erosion of an image with a kernel removes “islands” in the image smaller than the kernel. Used on binary images, it removes features that are smaller than the kernel and the edges of larger structures are cut-off. Letting $A \otimes B$ represent erosion of image A with kernel B , erosion can be defined as :

$$C = A \otimes B = \cap_{b \in B}(A)_{-b} \quad (5)$$

where $(A)_{-b}$ represents the translation of A by b . B can be visualized as a probe that slides across image A , testing the spatial nature of A at each point. Used on our binary map, the kernel moves over the entire dataset, image for image. It is centered on each pixel, where it checks whether the kernel completely overlaps the binary data. In the case of the 3×3 kernel, if the pixel and the surrounding pixels all have a value of 1, the pixel keeps the value 1. The 9 pixels of the kernel are the same as the 9 pixels over which it is laid in the dataset. If on the other hand, 1 or more pixels of the 9 pixels in the dataset are not 1, but 0, the pixel value is changed from 1 to 0 (if it had the value 1 to begin with). The effect is that features smaller than the kernel are completely removed and that the edges of larger features will be cut-off as well (table 2).

Dilation, on the other hand, of an image with a kernel fills ”holes” of a size equal to or smaller than the kernel. Used on binary images, dilation is the same as convolution. It enlarges features that are present in the data to the size of the kernel. Letting $A \oplus B$ represent dilation of image A with kernel B , dilation can be defined as :

$$C = A \oplus B = \cup_{b \in B}(A)_b \quad (6)$$

where $(A)_b$ represents the translation of A by b . When used on our binary map, the kernel moves again over the entire dataset, image for image. It is centered on each pixel, where it checks whether that pixel is 1 or 0. In the case of the 3×3 kernel, if the pixel has a value of 1, the pixel keeps the value 1 and all surrounding pixels become 1 if they are not 1 already. If, on the other hand, the pixel is 0, nothing happens. The effect is that features that are present are enlarged by the kernel. Also shown in table 2.

The erosion-dilation processing we carried out was the following:

$$R = (((BM \otimes K1) \oplus K1) \otimes K2) \oplus K2 \quad (7)$$

where BM is our binary map and R is our result. The combination of taking a low threshold value and using this erosion-dilation processing enabled us to get the BPs well-connected in time, BPs that merge or split show up and it removed much noise. Fig. 10 shows how the binary map transforms from a map with much noise to a map with only BPs.

3.4.2 Removing more noise

At this point there is still quite some noise left in our binary map. The previously mentioned reversed granulation and acoustic shocks are not entirely

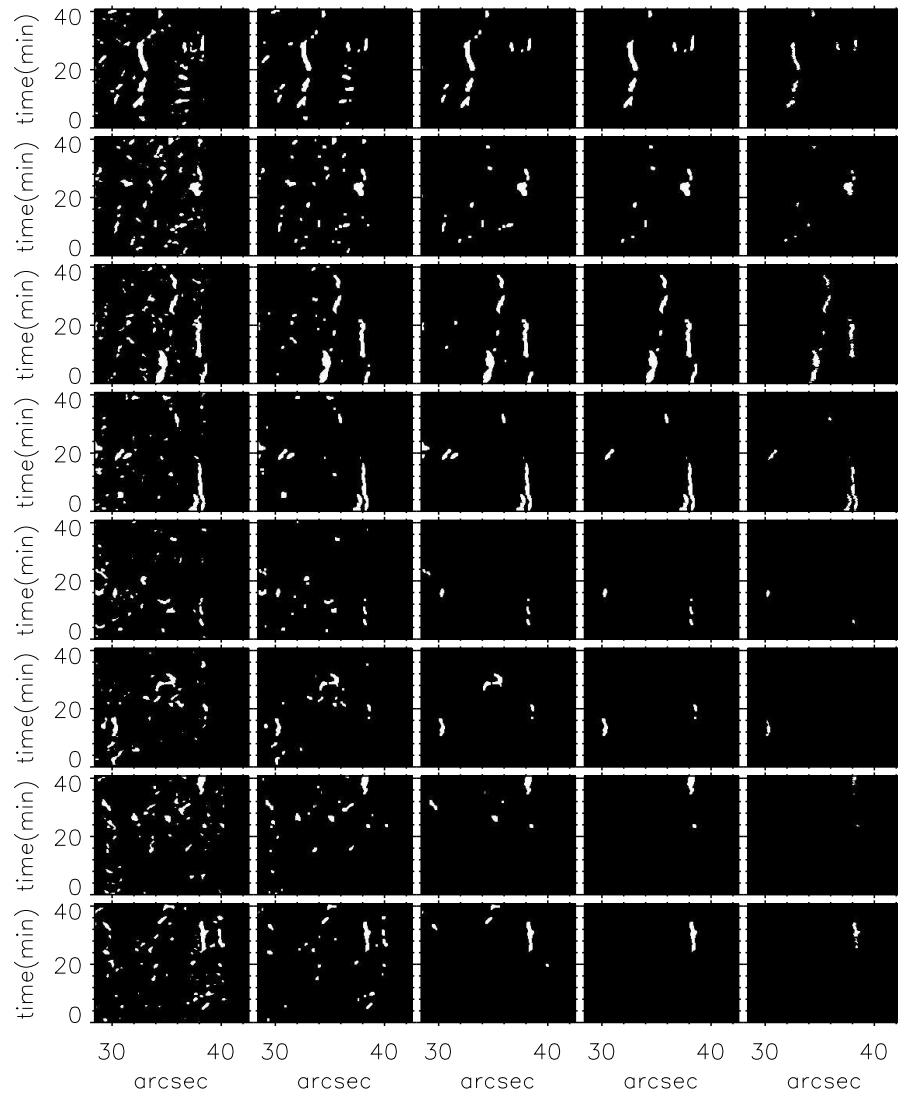


Figure 10: $x - t$ slices showing the transformation of a small part of the initial binary map with much noise to a map which only shows the BPs. The panels from left to right show the exact same area in the binary map and show the results from the different steps that we took to get a binary map with only BPs. From left to right: binary map after tres-holding, binary map after erosion-dilation processing, binary map after applying conditions on lifetime and size/shape of the BPs, binary map after manually removing the last noise, the end result after average thresholding. From top to bottom: different y -locations with steps of 6 pixels between them in increasing order.

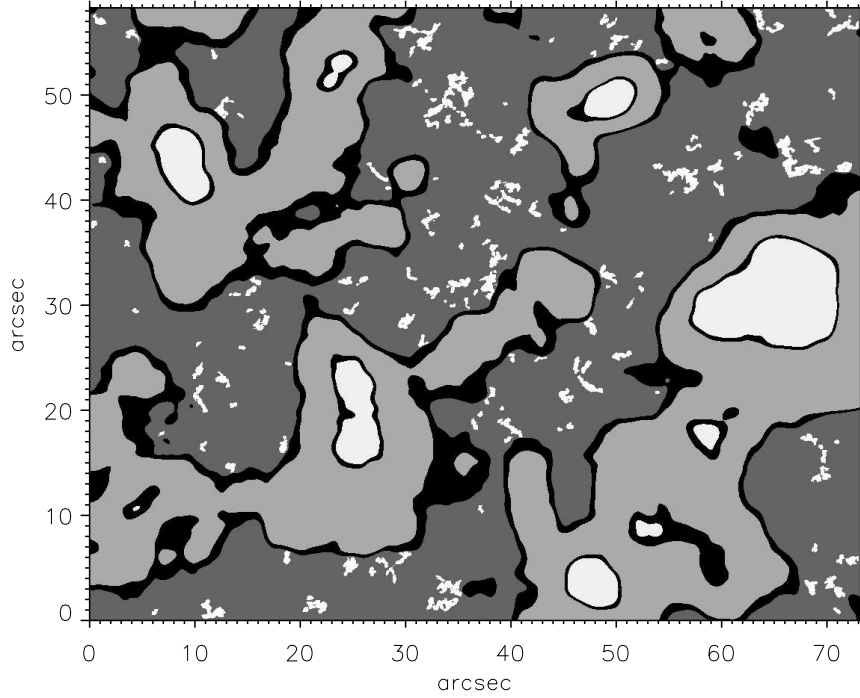


Figure 11: image showing the spatial location of all the BPs that were found in the Ca II H data during the entire time series. The IN, IM and NW masks are shown again as in Fig. 7. The white dots in the IN indicate the location of the BPs.

and arc-shaped elements.

The value of X_t , which represents the average size in the x direction $avg(X_{size})$, divided by the number of time steps T_{steps} is given by

$$X_t = \frac{avg(X_{size})}{T_{steps}} \quad (8)$$

and the condition is

$$X_t < 1.0. \quad (9)$$

The condition for Y_t is

$$Y_t < 1.0 \quad (10)$$

and its value is similar to X_t . So only if all three conditions are met, the feature is selected as a BP. The value of 1.0 for both X_t and Y_t had to be selected carefully by checking which would remove the most noise while retaining all the BPs.

We inspected the data visually at this point. There still were features that were not BPs. They were removed (Fig 10) to get a binary map with only BPs.

3.5 Identifying BPs

We can now assign an identity to each individual structure in the binary map to give each BP its own identity and we have their locations (x,y,t) . We removed BPs that were crossing the boundary of our mask, because they aren't suitable for analysis.

The result is a binary map of 188 BPs within the boundaries of the internetwork ready for analysis. Fig. 11 shows the spatial location of all the BPs during the entire time series. We clearly see a very patchy distribution of the BPs over the internetwork chromosphere.

4 Data reduction G band

The G-band BPs are more difficult to find, so we have a somewhat different approach in how we find these BPs. As mentioned before, the G-band BPs are smaller and live shorter on average when compared to the BPs in the Ca II H data. We do not need to produce a mask for this dataset for the internetwork, because the mask from the Ca II H dataset holds here as well. We start with performing a convolution of the data with the same kernel to enhance the BPs in the G band. We also used time-averaging and background removal to reduce the data. At this point we take another approach. We use the binary map of the Ca II H data to look for cospatial and cotemporal BPs in the G band. We then made a binary map again and we tried to remove as much noise as we could.

4.1 Convolution of G band data

Fig. 12 shows the result of performing convolution of the data with the 7x7 pixel kernel on the previously used subfield. We again see increased contrast in the G-band data for BPs. Besides that, the granules are clearly visible as homogeneous gray areas. The calculation is exactly the same as with the Ca II H data.

4.2 Time-averaging and removal of background

Since we are only interested in the BPs we can repeat the steps of time-averaging and the removal of the gray background again on the convoluted dataset. The result shows that all the granules are gone and that the BPs show more contrast with their surrounding. Again the calculations are exactly the same as with the Ca II H Data.

4.3 Dilation of binary map Ca II H BPs

Our result from the data reduction of Ca II H is the binary map with 188 BPs within the boundaries of the IN. We use this map to locate cospatial and cotemporal BPs in the G band. We must realize that the G-band samples the photosphere, whereas the Ca II H data samples the chromosphere, therefore the BPs are not exactly cospatial. The height difference between these regions is roughly 500 km. The magnetic fluxtubes move transversely through the atmosphere and they can be tilted with respect to the line of sight. The data show that BPs

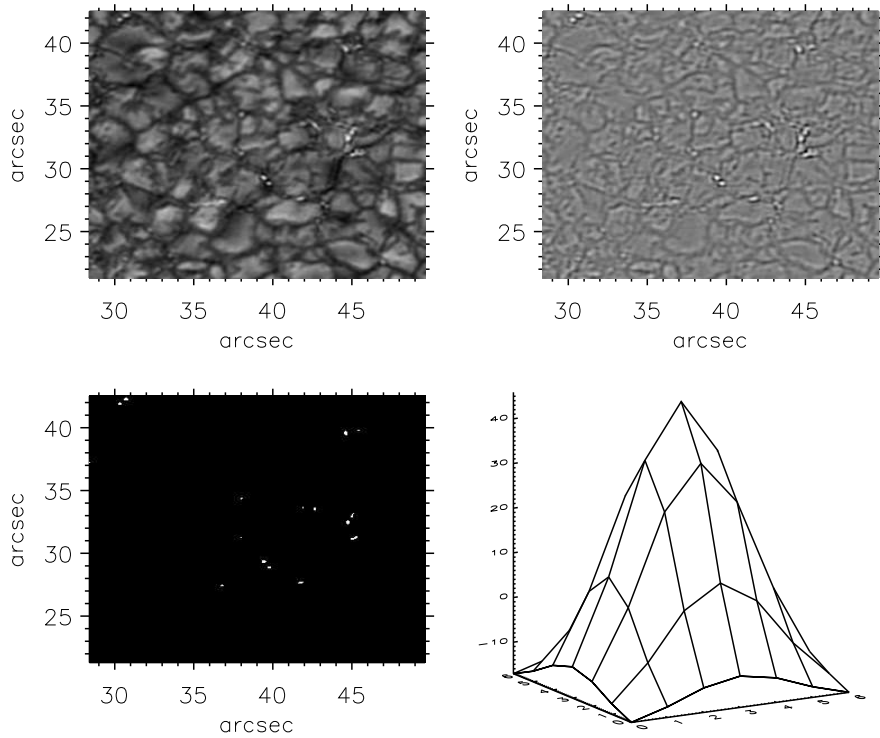


Figure 12: top left: same G-band image as in Fig. 2. Top right: G-band image after performing the convolution with the kernel which is shown bottom right. Bottom left: G-band image after convolution, time-averaging with previous and next images and after removing the gray background. Bottom right: kernel that we have used to perform a convolution with the original data to search for BPs. The kernel is 7×7 pixel² and has the form of the intensity distribution of an imaginary BP. The effect is that structures in the data that are similar to the shape of the kernel are enhanced, whereas other structures are flattened out

in Ca II H can start at a certain time step, while the BPs in the G-band data will start some time steps later or sooner. These time differences can be quite large. We chose to perform a dilation of the Ca II H binary map with a kernel that compensates for these differences between the datasets.

The kernel is a $7 \times 7 \times 70$ (x, y, t) pixel array filled with 1s. The result from the dilation of the Ca II H binary map is a binary map, with enlarged areas which also have enlarged lifetimes. This way we are certain that we are able to find all cospatial and cotemporal BPs.

4.4 Binary map of G-band data

The next step is to multiply this dilated Ca II H binary map with the the G-band data after having performed the convolution, time-averaging and removal of the background. We now have G-band data with cospatial and cotemporal BPs which we can find by thresholding the data again at a certain value to produce

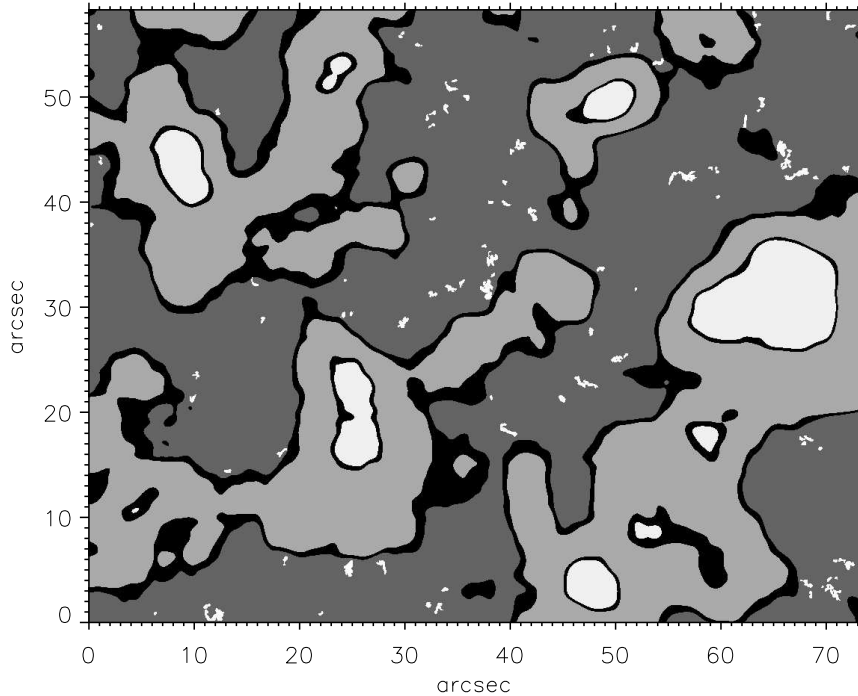


Figure 13: map of the spatial location of all the BPs found at the IN CaIIH BP locations in the G-band data during the entire time series. The IN, IM and NW masks are shown as in Fig. 7. The white dots in the IN indicate the location of the BPs.

a binary map of this data. We do not need to multiply it with our mask, since the Ca IIH binary map was already applied. As with the Ca IIH data, we had to be very careful in selecting the threshold value. We want all the BPs that are there and we want to have as little noise as we can in the binary map.

We did not use the erosion-dilation procedure as we did with the Ca IIH data, because it did not help to remove much noise in the G-band data. We do need to remove quite some noise, but we have limited the area in which we have to do this by only looking for cospatial and cotemporal BPs.

4.5 Removing noise and identifying BPs

We first removed these features that do not live longer than 192 seconds and also those that are not roughly circular. We used the same routine as with the Ca IIH data and the same conditions on lifetime and size or shape. After that, we also needed to remove quite some noise manually, which confirmed the fact that BPs are more difficult to find in the G band. We gave each BP its own unique identity and extracted their location information. We found 134 G-band BPs ready for analysis. Their spatial locations are shown in Fig. 13.

5 Analysis of Ca II H BPs

Since our code enhances the BPs in the data, the sizes of the BPs are too large. We correct for this by spatially averaging the BPs at each time step and removing those pixels that are below the average value. This reduces their size and gives it a more realistic size at each time step. Examples of this average thresholding are shown in Figs 10, 14 and 15. Also, the combination of a low threshold value and the erosion-dilation processing plays a vital role in being able to correctly determine the lifetime. It ensures that the BPs are correctly connected, whereas visual inspection would produce mistakes in estimating the lifetimes.

The next step in the BP analysis is checking which BPs are merging and splitting. Some examples of splitting or merging BPs are shown in Fig. 15. Correcting for such splitting and merging is vital to determine the average size and velocity of the BPs. We also checked which BPs are present at the beginning of the series and which BPs are still there when the series ends, these affect the lifetime distribution of the BPs.

5.1 Lifetime

Our analysis starts with measuring the lifetime of the BPs. As mentioned before we selected two subsets of the BPs. One set of BPs that do not merge or split and one set of BPs that start and end within the duration of the time series. The distribution of the complete set is biased. There are BPs that last during the whole time series and several BPs are present at the beginning of the series, whereas others are still there when the series ends. The distribution of the BPs that live between start and end of the series is therefore the best distribution. It is shown as a solid line in Fig. 16. This distribution consists of 134 BPs and has an average value of 9.9 minutes. The maximum of all three distributions is in the range of 3.0–4.6 minutes. The average lifetime of the BPs that do not split or merge is 8.7 minutes, whereas the whole set of BPs has an average of 11.4 minutes. A longer observation is necessary to determine the correct distribution.

5.2 Average diameter

The average diameter can also be evaluated from our binary map. The average thresholding ensured that we have correct values for the size of the BP at each time step. If the BP is strong at a certain time, the size will be large, whereas if the BP is weak, it will be small.

We calculated the average diameter of the BPs during their lifetime. 1 pixel corresponds to 51.5 km or 1 arcsec to 725 km. The average BP diameter is given by

$$D = 2 \times \sqrt{\frac{O}{\pi}} \quad (11)$$

where D is the diameter and O the surface. The distribution of the BPs that begin and end within the temporal boundaries of the dataset is shown by a solid line in Fig. 16. Its average value is 209 km and the maximum of the distribution

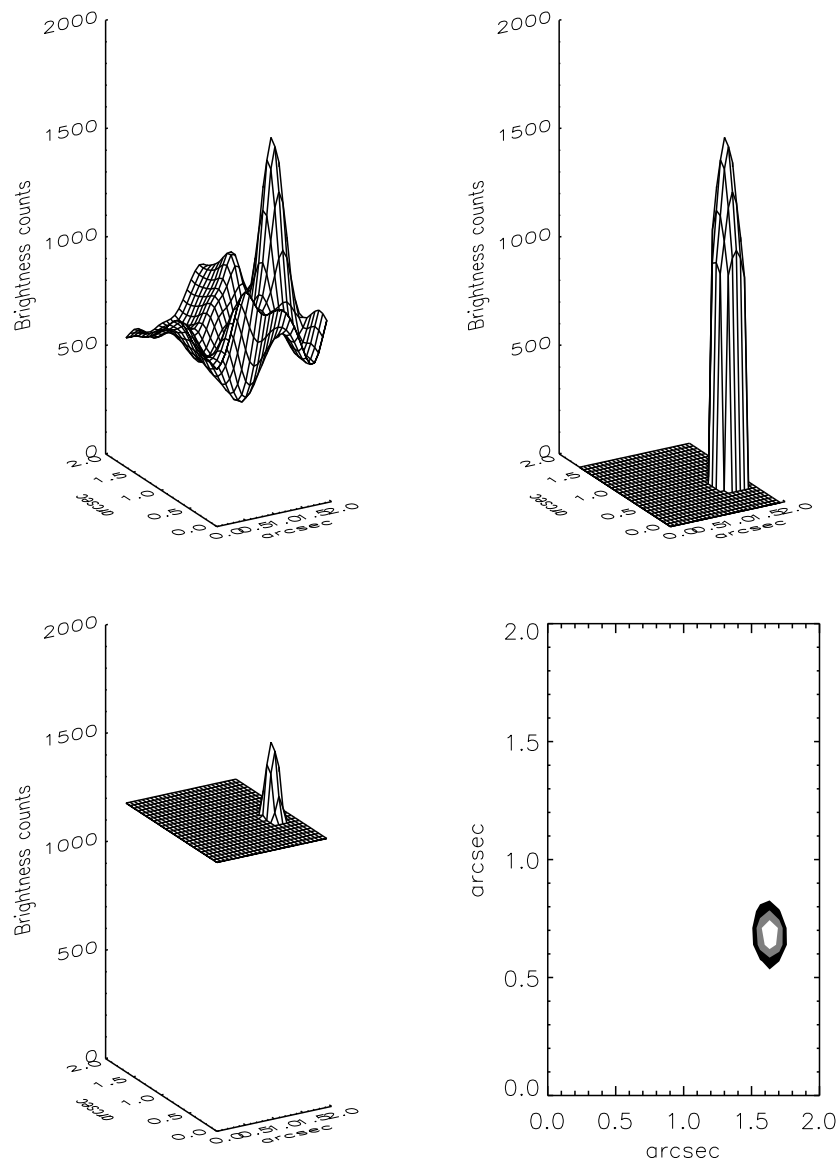


Figure 14: average thresholding on a BP at a certain time step. Top left: surface plot of intensity distribution of an area of $2 \times 2 \text{ arcsec}^2$ from the original data. Top right: surface plot (same area) of intensity distribution of the original data multiplied with the binary map, thus only showing the BPs. Bottom left: same as top right surface plot, but thresholded at the average value of the pixels that are not 0 in the top right surface plot. Everything above this threshold value is the BP as one can observe in this surface plot. Bottom right: contour plot showing the size and shape of the BP at that time step.

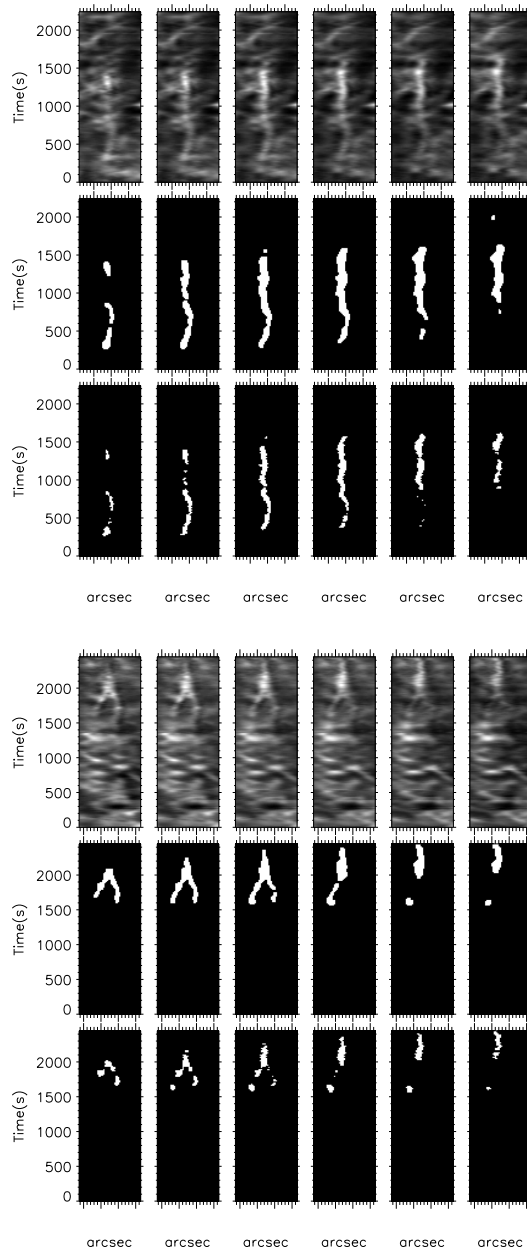


Figure 15: $x - t$ slices of 2 BPs showing their development in time. From left to right: increasing y -coordinate with increments of 1 pixel. Upper half from top to bottom: original data of a BP that doesn't split or merge, same area in the binary map before average thresholding, same area in the final binary map. Lower half: original data of a BP that merges, same area in the binary map before average thresholding, same area in the final binary map. The large x -axis tick-marks correspond to 1 arcsec intervals.

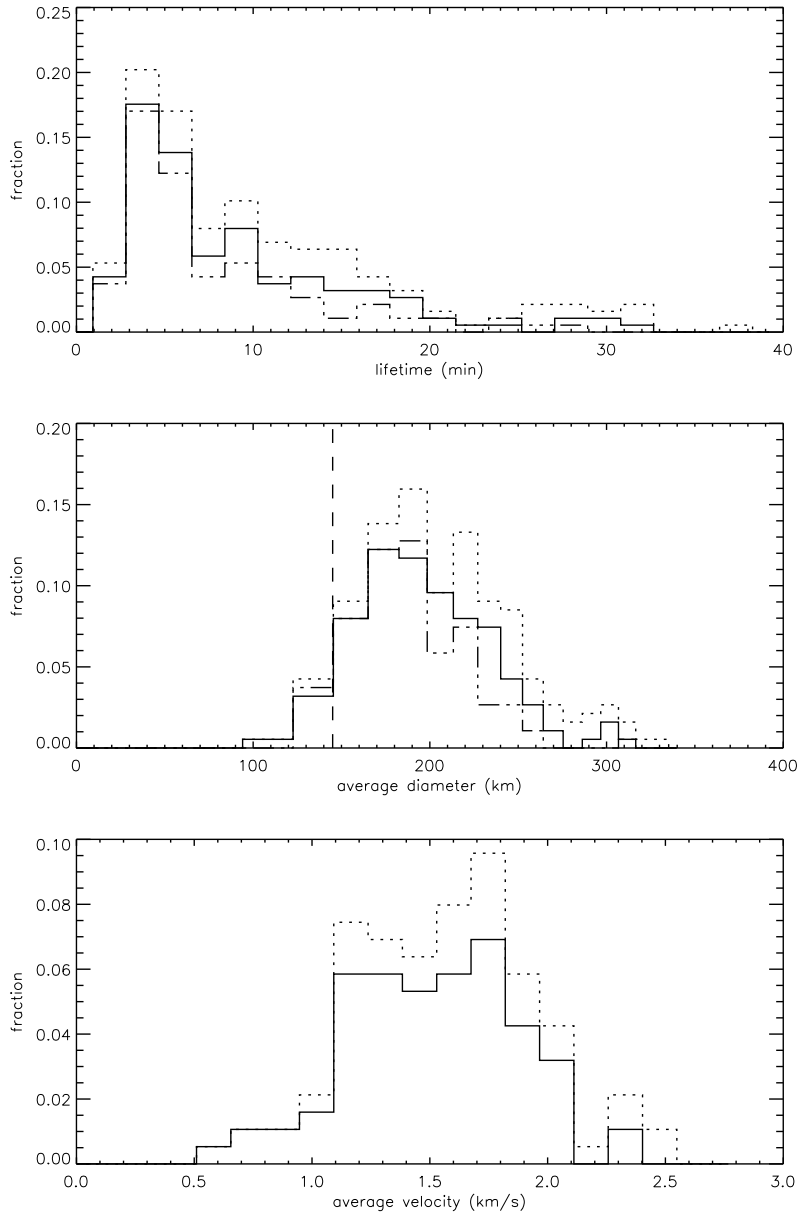


Figure 16: histograms of lifetime, average diameter and average velocity of the BPs in the chromosphere. Top: histogram of lifetime, the solid line shows the distribution of the BPs that start and end within the complete time series. The dotted line shows the complete distribution and the dashed-dot-dot line shows the distribution of those BPs with similar curve coding that do not split or merge. Middle: histogram of average diameter, with similar line coding. The dashed vertical line indicates the angular resolution limit of the telescope. Bottom: histogram of average velocity. The dashed line is the set of BPs that do not split or merge. The solid line represents the set of BPs that do not split or merge and that are within the temporal boundaries of the dataset.

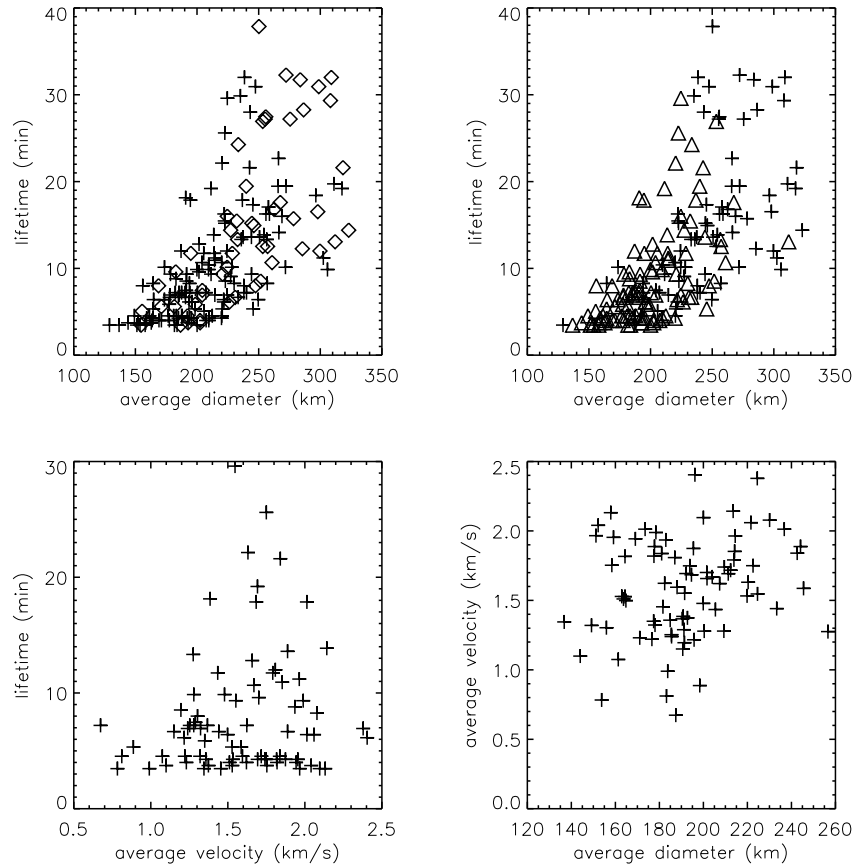


Figure 17: scatter plots of BP lifetimes, average diameters and average velocities. Top left: lifetime versus average diameter. The + signs indicate the set of BPs that start and end within the time series. The squares represent the points that are present at the beginning and end of the time series. Top right: lifetime versus average diameter, the set of BPs that do not split and/or merge are indicated by the + signs. The triangles represents the splitters and mergers. Bottom left: lifetime versus average velocity, only the BPs that do not split or merge and that start and end within the time series are shown. Bottom right: average velocity versus average diameter, only showing those BPs that do not split or merge and that start and end within the time series.

is in the range 166–182 km. The complete set of BPs has on average an average diameter of 219 km and the set of BPs that don't merge or split has an average of 199 km. The maximum of their distribution is in the range of 182–198 km. The angular resolution limit of the telescope (0.2 arcsec or 145 km) is indicated by the dashed vertical line. The peak values of all three distributions are above the angular resolution limit of the telescope which indicates that there probably are not much BPs that have sizes smaller than 145 km in the chromosphere.

5.3 Average velocity

To calculate the velocities of the BPs we need to know their exact locations. We chose to use a routine that calculates the center of intensity distribution per time step and identifies that location as the position of the BP. For each BP, we calculate the center-of-mass of its position in the binary map multiplied with its intensity distribution, hence center of intensity distribution. We tracked the movement of this position during the entire lifetime of the BP and divided this total distance by the lifetime of the BP, which gives an average velocity of the BP during its lifetime. We calculated this for the set of BPs that do not split and/or merge and its subset of BPs that do not split or merge and are within the temporal boundaries of the data. The average velocity of the first mentioned set is 1.6 km/s and the maximum of the distribution is in the range of 1.67–1.81 km/s. The average velocity of the set of BPs that are within the temporal boundaries and do not split or merge is 1.6 km/s and the maximum of the distribution is in the same range of 1.67–1.81 km/s.

5.4 Possible relations ?

We produced scatter plots (Fig. 5) of these different characteristics to check whether there are possible relations between them. The first two scatter plots show their lifetime versus average diameter. The first shows the subset of BPs that start and end within the time series and the subset of BPs that are present at the temporal boundaries. The second shows the division in splitting and/or merging BPs against non-splitting and non-merging BPs.

We observe that most BPs have lifetimes of 3–7 minutes and that their average diameter is between 130–220 km. BPs that exist for more than 11 minutes all have diameters larger than 180 km. So, if a BP is relatively large, it has a relatively long lifetime. Most of the BPs that are present at the temporal boundaries of the dataset have relatively large lifetimes and are relatively large. The set of BPs that split and/or merge show relatively long lifetimes, but their sizes are smaller compared to other BPs that have the same duration.

There is no clear relation between lifetime and average velocity. BPs with a short lifetime span the entire range of velocities, whereas BPs with long lifetimes are more centered towards the average value of the velocities. One expects this since the average velocities come from dividing the total distances traveled by lifetimes. This scatter plot tells us that for short-lived BPs there is no relation with their average velocities and that long-lived BPs have average velocities near the average value of the entire set of BPs.

It is interesting to test whether there is a relation between the average velocity and the average diameter of BPs. The scatter plot shows more or less two regions. Almost all BPs with a diameter smaller than 200 km have average

velocities from 0.7–2.2 km/s and those with diameters larger than 200 km have velocities of 1.3–2.6 km/s. One could argue from this that the larger the BP, the faster it can move in the chromosphere. The relation is however not very clear.

5.5 Intensity profiles and wavelet analysis

We were also interested in possible periodicities in the intensities of the BPs, so we produced intensity profiles for the BPs that do not split or merge and then performed a wavelet-analysis on these intensity profiles to check whether there are significant periodicities. We show some examples of intensity profiles of BPs and their corresponding wavelet-analysis. We only did the wavelet analysis on BPs that live longer than 800 seconds, because shorter-lived BPs do not show significant periods. We have analyzed 17 BPs of which 8 show significant periods.

Figs 18 and 19 show the intensity profile and wavelet analysis of four BPs that do not merge and/or split, that show significant periods. The wavelet analysis shows how significant certain periods are during certain intervals of the duration of the BP. The black regions indicate periods with a 95% level of confidence. The area free from hatching is the “cone of interest”. Anything below the cone is uncertain. So the first BP shows possible significant periods of 180 and 300 seconds which are just below the cone. The second BP shows a significant period around 200 seconds, which is within the “cone of interest”. The analysis on the third BP gives a significant period around 220 seconds, whereas the fourth shows a period around 300.

6 Analysis of G-band BPs

6.1 Lifetime

The lifetime distribution of the BPs that are within the temporal boundaries (solid line lifetime Fig. 20) shows an average value of 7 minutes and the maximum of the distribution is in the range of 2.8–4.7 minutes. The complete set of BPs has an average of 8.1 minutes and the maximum of the distribution is in the same range of 2.8–4.7 minutes. The set of BPs that do not merge and/or split has an average of 6.5 minutes and the maximum of the distribution lies again in the range of 2.8–4.7 minutes. These values are again biased for the same reasons mentioned in the previous chapter and adding to that the fact that we have only looked for cospatial and cotemporal BPs, i.e. we have not analyzed the complete set of BPs in our G-band dataset. The best distribution is again the one of the BPs that are within the temporal boundaries of the data. A longer observation with the Dutch Open Telescope should give better results.

6.2 Average diameter

The average diameter distribution for the set of BPs that are within the temporal boundaries shows an average value of 171 km and the maximum of the

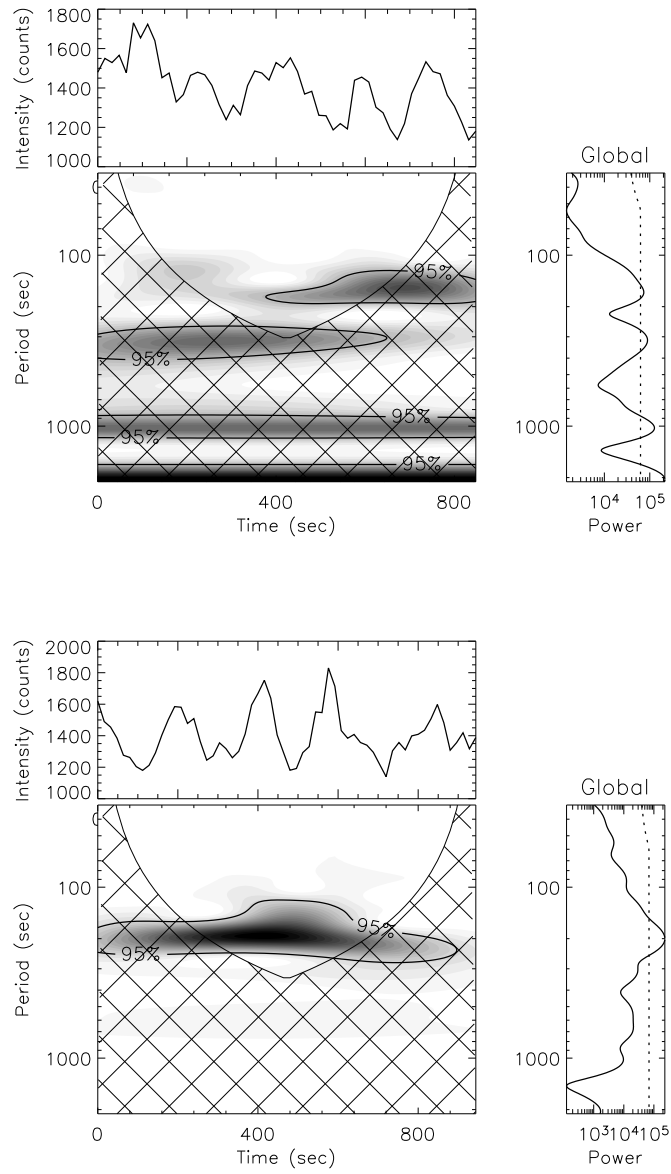


Figure 18: wavelet analysis of two Ca II H BPs. For each BP, its intensity profile is shown at the top. Below the profile, the frequency analysis is shown with the cone of interest. On the right hand side is the global power shown for the frequency domain that is relevant. The dashed line indicates the 95% confidence level. Top: this BP shows possible significant periods around 180 and 300 seconds. Bottom: a BP showing a significant period around 200 seconds.

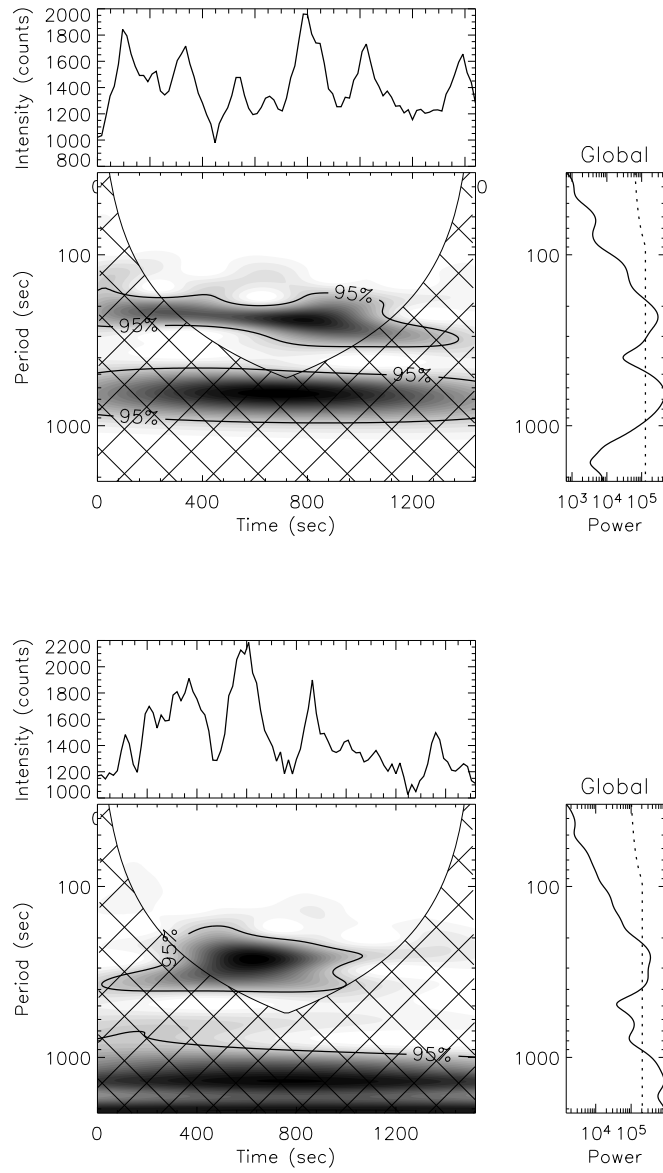


Figure 19: wavelet analysis of two Ca II H BPs. For each BP, its intensity profile is shown at the top. Below the profile, the frequency analysis is shown with the cone of interest. On the right hand side is the global power shown for the frequency domain that is relevant. The dashed line indicates the 95% confidence level. Top: this BP shows a significant period around 220 seconds and a possible period around 700 seconds which is very uncertain. Bottom: a BP showing a significant period around 300 seconds, ranging over 200–400 seconds.

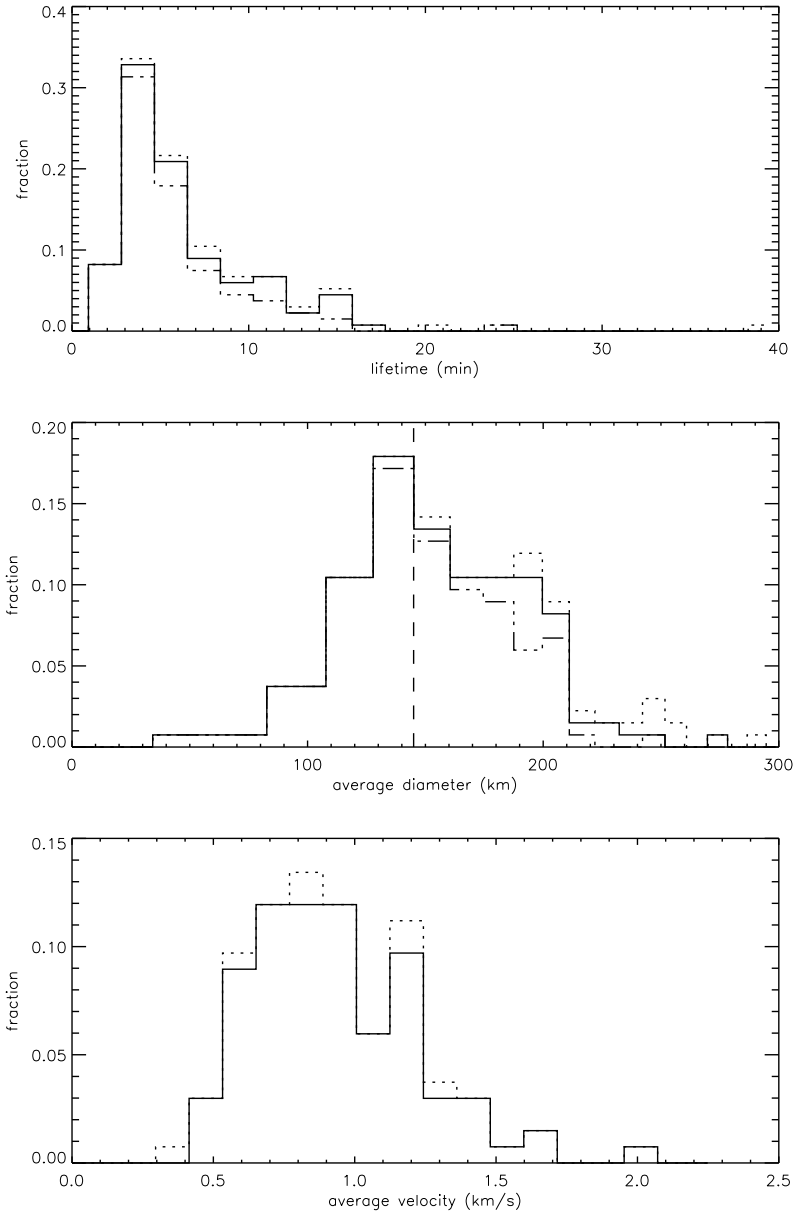


Figure 20: histograms of lifetime, average diameter and average velocity of the BPs in the photosphere. Top: lifetime histogram. The solid line shows the distribution of the BPs that start and end within the complete time series, the dotted line shows the complete distribution, and the dashed-dot-dot line shows the distribution of the BPs that do not split or merge. Middle: histogram of average diameter, with similar line coding. The dashed vertical line indicates the angular resolution limit of the telescope. Bottom: histogram of average velocity. The dashed line is the set of BPs that do not split or merge and the solid line is the set of BPs that do not split or merge and that are within the temporal boundaries of the data set.

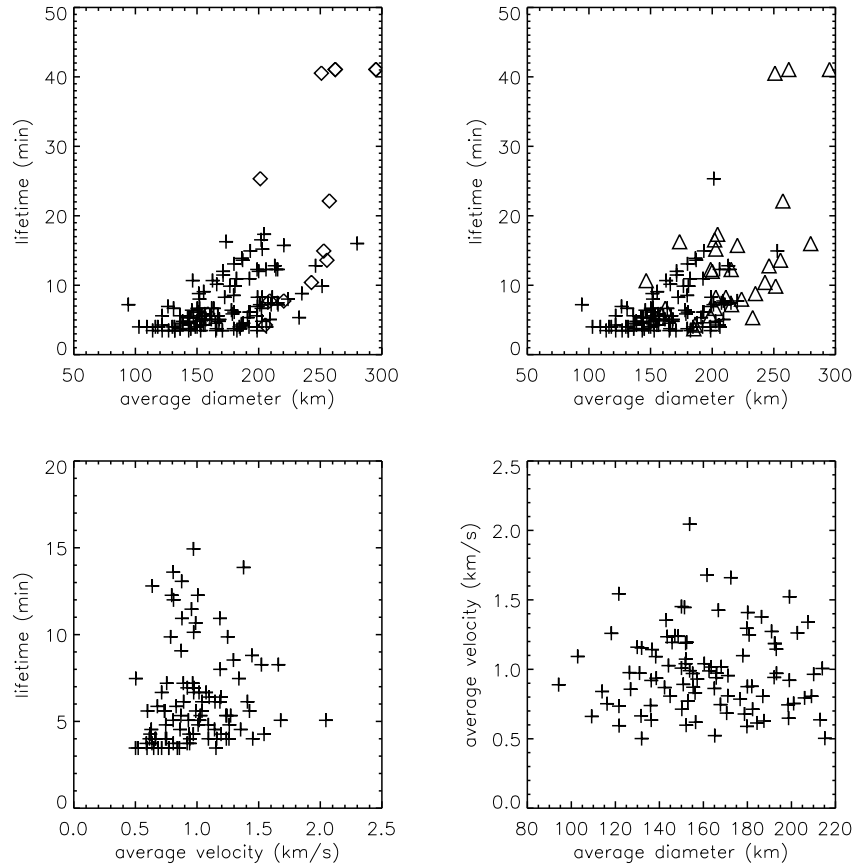


Figure 21: scatter plots of BP lifetimes, average diameters and average velocities. Top left: lifetime versus average diameter. The + signs indicate the set of BPs that start and end within the time series. The squares represent the points that are present at the beginning and end of the time series. Top right: lifetime versus average diameter, the set of BPs that do not split and/or merge are indicated by the + signs. The triangles represent the splitters and mergers. Bottom left: lifetime versus average velocity, only the BPs that do not split or merge and that start and end within the time series are shown. Bottom right: average velocity versus average diameter, only showing the BPs that do not split or merge and that start and end within the time series.

distribution is in the range of 129–145 km. The complete set of the BPs has an average of 176 km and the maximum lies in the same range of 129 – 145 km. Finally, the set of BPs do not split and/or merge has an average of 165 km with a maximum also in the range of 129–145 km. We did not need to apply average thresholding, because the size of the BPs is correct due to the threshold-value, the calculation was similar to that of the Ca II H BPs. The angular resolution limit of the DOT is shown again as the dashed vertical line. All three distributions peak near this limit, which suggests that there probably are much more BPs with sizes smaller than 145 km which we do not observe since they are too small. The real distribution will probably have its peak values below 145 km. This shows that G-band BPs are more difficult to find.

6.3 Average velocity

The set of BPs that exist only within the temporal boundaries of the data shows an average value of 1.0 km/s for the average velocity. The distribution peaks in the range of 0.76–0.88 km/s. The set of BPs that do not split and/or merge and that are within the temporal boundaries also has an average value of 1.0 km/s and the distribution peaks in the same range. We again used the same method in our calculation as with the Ca II H BPs, using the center of the intensity distribution as the exact location of the BP.

6.4 Possible relations ?

The scatter plots (Fig. 21) showing the lifetime versus average diameter of the BPs shows that almost all BPs live shorter than 20 minutes. BPs that have lifetimes shorter than 10 minutes cover the range of 100–250 km for the average diameter. The BPs that live longer than 10 minutes all have average diameters larger than 150 km, indicating that there might be a relation of lifetime versus size. Notice that almost all of the BPs that are at the temporal boundaries are relatively large and have lifetimes in the range of 10–40 minutes. The BPs that split and/or merge show a somewhat similar trend. Most live longer than 10 minutes and are relatively large.

The relation between average velocity and lifetime is not clear. Short-lived BPs cover the entire range of average velocities, whereas long-lived BPs are more centered towards the average value of 1,0 km/s. Again this can be explained in the same way as with the Ca II H BPs. There is no apparent relation.

The last scatter plot shows average diameter versus average velocity and shows that BPs that move relatively slow cover the entire range of average diameters. There is no apparent relation as there seems to be with the Ca II H BPs in this aspect.

6.5 Intensity profiles and wavelet analysis

We produced intensity profiles for all G-band BPs and performed a wavelet analysis on these to see whether there are significant periods in the intensities of the BPs. Only 5 BPs that do not split and/or merge and live longer than 800 seconds were found in the G-band data. All 5 show no significant period, 2 of them are shown in Fig. 22. The other BPs that do not split and/or merge are too short-lived to perform a wavelet-analysis.

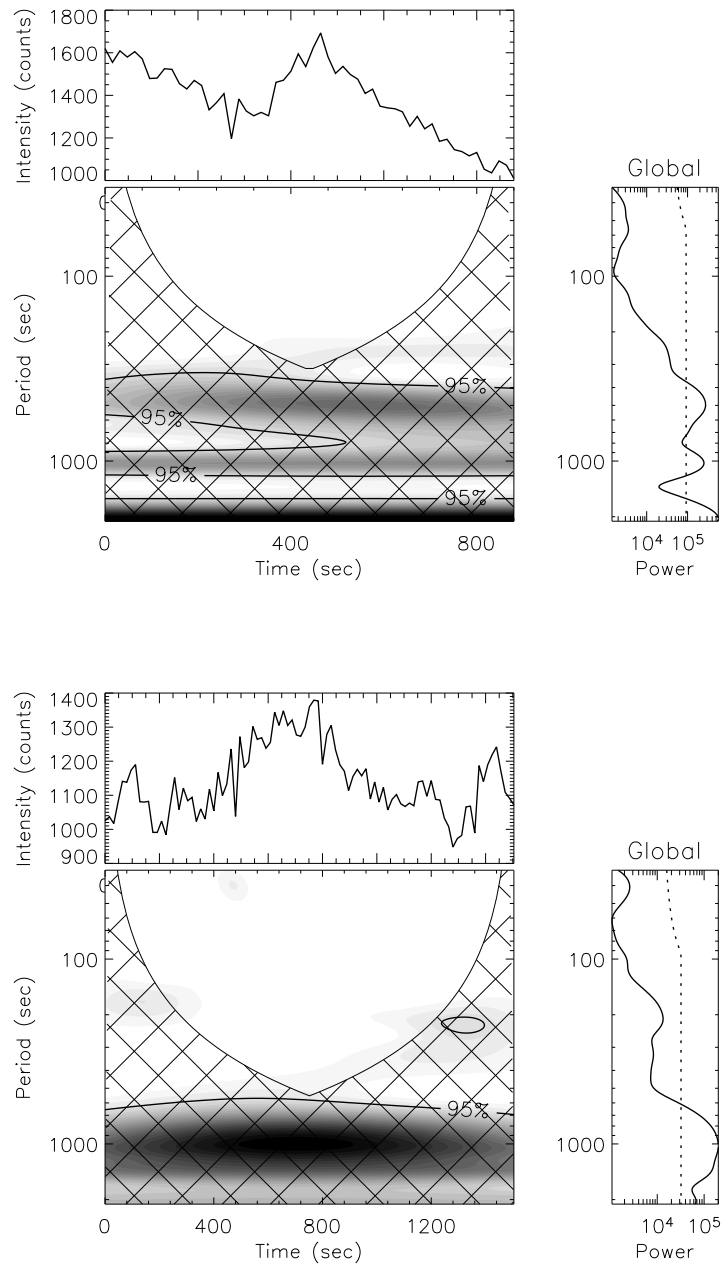


Figure 22: wavelet analysis of two G-band BPs. For each BP, its intensity profile is shown at the top. Below the profile, the frequency analysis is shown with the “cone of interest”. On the right hand side is the global power shown for the frequency domain that is relevant. The dashed line indicates the 95% confidence level. No significant period is found.

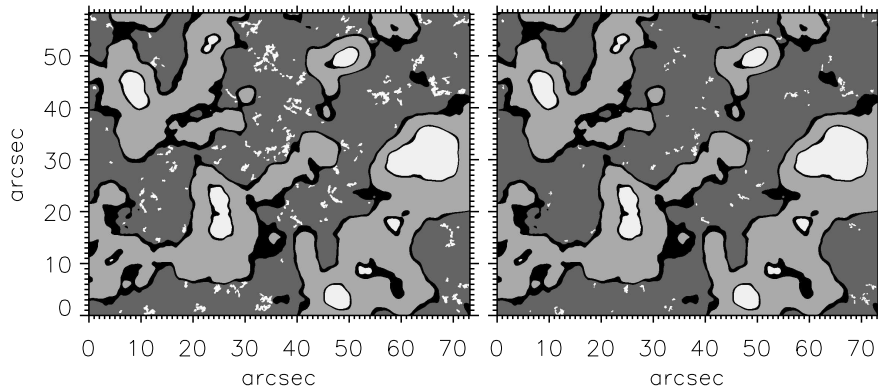


Figure 23: spatial locations of the BPs in the internetwork. Left: Ca II H data. Right: G-band data. These are the same images as in Figs 11 and 13.

7 Cospatial and cotemporal BPs

We started our analysis with the BPs in the chromosphere and then located cospatial and cotemporal BPs in the photosphere. Fig. 23 shows the spatial locations of the BPs in the Ca II H and G-band data. One can see that the locations of the BPs in the internetwork chromosphere are limited to certain areas. Their distribution over the internetwork is very patchy. Some areas of the internetwork do not show BPs during the whole duration of the observations. The locations of the BPs in the G-band data clearly show that they are to a high degree cospatial.

We calculated for all BPs, whether the Ca II H BPs have a cospatial and cotemporal partner in the G band. We used the final binary maps of both datasets to see if there is an overlap between them. If we just look at overlap in the sense that in both binary maps certain pixels must be 1, at the same x, y, t location both binary maps must be 1, we find that 108 of the 134 G-band BPs are partners with Ca II H BPs (81%). From 188 Ca II H BPs, 116 BPs do not have a partner in the G-band. Some Ca II H BPs have more than 1 partner, even up to 5. For these Ca II H BPs that have more than 1 partner, we noticed that sometimes the corresponding G-band BPs also have other Ca II H BPs as their partners. If we take this into account as well, only 36% of the Ca II H BPs have 1 partner or more.

However, if we do not require exact pixel overlap for the corresponding BPs but allow for spatial and temporal differences of 2 pixels in each direction (x, y, t) , then 95% of the G-band BPs have partners in the Ca II H data and 40% of the Ca II H BPs have a partner in the G band.

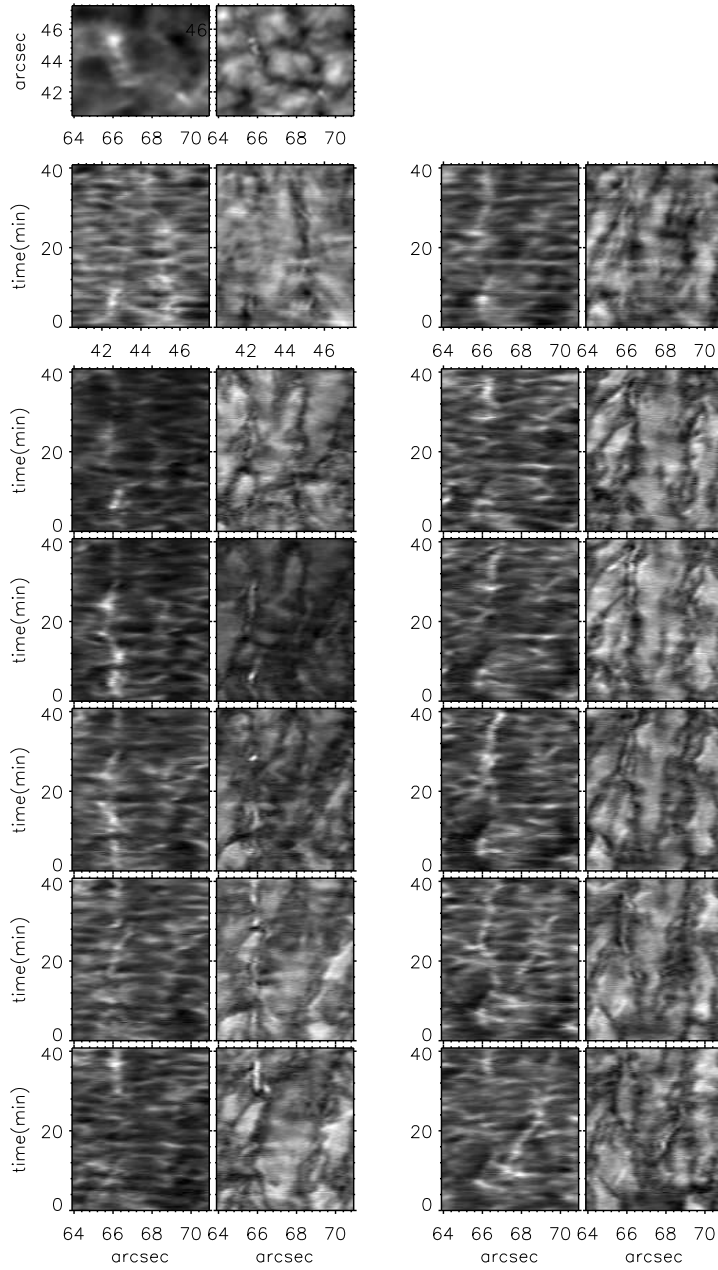


Figure 24: cospatial and cotemporal BPs in Ca I H and G band. The x -range of the area that is shown is 64–72 arcsec and the y -range is 40.5–47.5 arcsec during the whole observation. Top left: $x - y$ images summed over the whole observation. Second left: $y - t$ slices summed over the x -range under consideration. First right: $x - t$ slices summed over the y -range under consideration. The rest of the images from top left to top right to bottom left to bottom right are individual $x - t$ slices with increments for the y -coordinate of 4 pixels or 0.28 arcsec. For each column: on the left Ca I H, on the right G band. Fig. 25 shows the same locations in the binary maps.

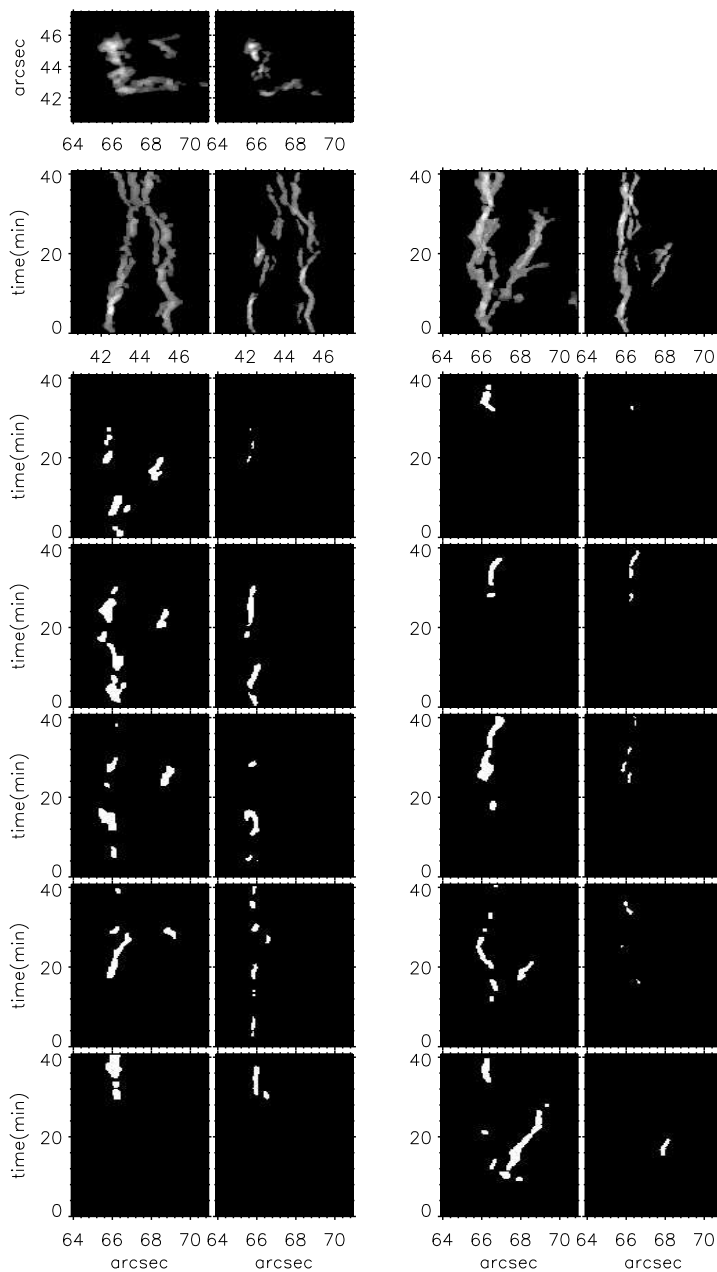


Figure 25: cospatial and cotemporal BPs in the Ca II H and G-band binary maps. The x -range of the area that is shown is 64–72 arcsec and the y -range is 40.5–47.5 arcsec during the whole observation. Top left: $x - y$ images summed over the whole observation. Second left: $y - t$ slices summed over the x -range under consideration. First right: $x - t$ slices summed over the y -range under consideration. The rest of the images from top left to bottom left to top right to bottom right are individual $x - t$ slices with increments for the y -coordinate of 4 pixels or 0.28 arcsec. For each column: on the left Ca II H, on the right G band.

An extraordinary example of a Ca II H BP with several partners in the G band of which some have several partners in Ca II H is shown in Figs 24 and 25. The region that is shown spans over $x = 64 - 72$ arcsec, $y = 40.5 - 47.5$ arcsec and the complete time sequence. Several BPs are seen in the Ca II H and G-band data of which most are partners of each other. The images of $x - t$ summed over the y direction and $y - t$ summed over the x direction show that these BPs as a group have a long lifetime, whereas the individual BPs have shorter lifetimes. The example is shown to indicate that some patches of individual BPs do have longer lifetimes than the calculations reveal. Visual inspection of the data indicates this as well. The $x - y$ images show the path that the BPs follow. The G-band image shows a dark intergranular lane during the whole observation.

8 Discussion

The results show that BPs on average have longer lifetimes (9.9 minutes) in the chromosphere than in the photosphere (7.0 minutes). This is not a significant difference. It indicates the already mentioned fact that BPs in the G band are more difficult to find. The distribution of all the BPs that are within the temporal boundaries peaks in the range of roughly 3.0–4.5 minutes for both datasets. This indicates that BPs overall have short lifetimes and the time scale is similar to that of granular dynamics. BPs that live relatively long however do occur frequently enough to give an average value of about 2 times the maximum of the distribution in the chromosphere and photosphere.

The average diameter of the BPs that do not merge or split is 199 km in the chromosphere compared to 165 km in the photosphere. The complete sets show average values of 219 km (Ca II H) and 176 km (G band), whereas the set of BPs that are within the temporal boundaries show values of 209 km (Ca II H) and 171 km (G band). Thus BPs on average are roughly 17% larger in the chromosphere when compared to the photosphere. The distribution of the different sets peaks roughly in the range of 170–200 km for the Ca II H data, whereas the G-band data peaks in the range of 130–145 km. The peak values of the Ca II H distributions lie above the angular resolution limit of the DOT which indicates that these distributions approach the real distribution. The G-band distributions however have their peak near the angular resolution limit. The part of the distributions that is on the right of the limit is therefore real, but the part on the left is just from the angular resolution limit. There probably are more BPs with average diameters smaller than 145 km which we just can not find. All of this clearly shows that the chromospheric BPs are larger than the photospheric BPs and that the Ca II H BPs are easier to find.

It is interesting to notice that the average value for the average velocity of the BPs in the chromosphere is quite a bit larger than its value in the photosphere, its 1.6 km/s compared to 1.0 km/s. Even more so, the distribution in Ca II H peaks at a higher value, i.e. in the range of 1.65–1.80 km/s. The maximum in the G-band distribution is lower than its average, it peaks in the range of 0.75–0.90 km/s. So on average they move quite a bit faster in the chromosphere, but most of them move about twice as fast in the chromosphere when compared to the G-band data. Together with their size, these velocities show that the fluxtubes are more constrained in the photosphere due to the higher gas pressure

surrounding them.

The scatter plots for lifetime versus average diameter show a trend in the sense that BPs that live relatively long have relatively large diameters. The scatter plots of lifetime versus average velocity do not show a possible relation. Maybe in the chromosphere there is a relation of average velocity versus average diameter in the sense that the larger the BP, the faster it moves. But the BPs that live relatively short do have velocities from 0.5–2.2 km/s. The G-band BPs show no relation at all for these two characteristics.

The wavelet analysis showed significant periods in the range of 200 – 400 seconds for chromospheric BPs that do not split and or merge, but also showed that this only holds for half of the BPs that were considered in this analysis. The other BPs did not show periods at all. Non of the G-band BPs showed a significant period.

Our identification of cotemporal and cospatial BPs showed that most of the BPs in the G band have a Ca II H partner (80–95 %, depending on how strict we are in assigning partners). Vice versa, the Ca II H BPs only have in 36 to 40% of the cases a partner in the photosphere. Ca II H BPs are more frequent and often have several partners in the G-band data. The patchy distribution of the BPs over the chromospheric internetwork indicate mesogranular time scales for these patches. This raises the question whether local convection dynamos below the surface are responsible for these patches of magnetic fluxtubes.

9 Conclusion

The results show that the Ca II H BPs are easier to find than the G-band BPs. The lifetimes of the BPs in the G band show a similar distribution as the analysis of Sanchez Almeida et al. (2004). It shows a time scale corresponding to that of granular dynamics.

Figs 24 and 25 show an example of 3 Ca II H BPs that are cospatial and cotemporal with 5 G-band BPs. The images of $x - t$ summed over the y direction and $y - t$ summed over the x direction show their connection and we are convinced that although we find several BPs in this area, they all form a large group manifestating much magnetic activity during the whole time sequence. This is another bias in our lifetime distribution. The example is an extraordinary one, but is shown to indicate that BPs on occasion fade out and reappear later, both in chromosphere and photosphere. Visual inspection of the data reveals that there are a number of BPs that seem to last longer than our calculations can pickup, due to their flashing nature. The $x - y$ images show the path that the BPs follow. They move in an intergranular lane during the complete time sequence, shown in the G band image, which indicates much longer time scales for these magnetic field patches than the granular time scales that are found for the individual BPs.

The size and velocity of the BPs in both chromosphere and photosphere indicate that the fluxtubes are really moving around in the chromosphere when compared to the photosphere. Their movement is restricted by the granulation surrounding them in the photosphere when compared to the environment in the chromosphere. That can also explain their difference in size.

BPs in the chromosphere and photosphere have relatively large diameters when they live relatively long.

The wavelet analysis did not reveal any significant periods in the intensities of the BPs for the photospheric ones. Half of the chromospheric ones revealed periods around 200 – 400 seconds. Maybe this is from superposition from the background on the intensity of the BPs or it is a real signal. It needs to be investigated further.

Furthermore, we conclude that if there is a G-band BP, there probably is one in the overlying chromosphere. However, if there is Ca II H BP, the probability of finding one in the photosphere is only 0.4. Probably, because the G-band BPs are harder to find. They are smaller and their contrast in the G-band data is not as good as in the Ca II H data. Their size can be smaller than the angular resolution limit of the telescope and therefore we can not observe them.

Acknowledgment

This research was done under the supervision of Rob Rutten, Peter Sütterlin and Kostas Tziotziou in order to receive my Masters degree in astrophysics. In addition to them, I also received much help from Alfred de Wijn. I am very grateful to them in making this research possible and successful. I wish the entire solar physics group at the Sterrenkundig Instituut Utrecht much success, now and in the future.

References

- [1] Bellot Rubio, L. R.; Rodrguez Hidalgo, I.; Collados, M.; Khomenko, E.; Ruiz Cobo, B. 2001, *ApJ*, 560, 1010
- [2] Bellot Rubio, L. R.; Collados, M. 2003, *A&A*, 406, 357
- [3] Berger, T. E., Schrijver, C. J., Shine, R. S., Tarbell, T. D., Title, A. M., Scharmer, G., 1995, *ApJ*, 454, 531
- [4] Berger, T. E., Title, A. M., 1996, *ApJ*, 463, 365
- [5] Berger, T. E., Löfdahl, M. G., Shine, R. S., Title, A. M., 1998, *ApJ*, 495, 973
- [6] Berger, T. E.; Löfdahl, M. G.; Shine, R. A., Title, A. M., 1998, *ApJ*, 506, 439
- [7] Bettonvil, F.C.M., Hammerschlag, R.H., Sütterlin, P., Jägers, A.P., & Rutten, R.J. 2003, in *Innovative Telescopes and Instrumentation for Solar Astrophysics*, ed. S. L. Keil & S.V. Avakyan, *Procs. SPIE* 4853, 306
- [8] Hale, G.E., Ellerman F., 1904, *ApJ*, 19, 41
- [9] Hasan, S.S., 1983, *AUS*, 102,73
- [10] Hasan, S.S., 1984, *ApJ*, 285,851
- [11] Hasan, S.S., 1985, *A&A*, 143, 39
- [12] Hasan, S.S., 1986, *MNRAS*, 219, 357
- [13] Kerswell, R., Childress, S., 1992, *ApJ*, 385, 746
- [14] Krijger, J. M., Rutten, R. J., Lites, B. W., Straus, Th., Shine, R. A., Tarbell, T. D., 2001, *A&A*, 379, 1052
- [15] Langhans, K., Schmidt, W., 2002, *A&A*, 382, 312
- [16] Langhans, K., Schmidt, W., Rimmele, T., 2002, *svco.conf*, 397
- [17] Löfdahl, M. G., Berger, T. E., Shine, R. S., Title, A. M., 1998, *ApJ*, 495, 965
- [18] Nisenson, P., van Ballegooijen, A. A., de Wijn, A. G., Stterlin, P., 2003, *ApJ*, 587, 458
- [19] Nordlund, A., 1983, *AUS*, 102, 79
- [20] Parker, E. N., 1978, *ApJ*, 221, 368
- [21] Rajaguru, S. P., Kurucz, R. L., Hasan, S. S., 2002, *ApJ*, 565, 101
- [22] Roberts, B., Webb, A. R., 1978, *SoPh*, 56, 5
- [23] Rutten, R. J., Kiselman, D., Rouppe van der Voort, L., Plez, B., 2001, *aspt.conf*, 445

- [24] Rutten, R. J., Hammerschlag, R. H., Bettonvil, F. C. M., Sütterlin, P., de Wijn, A. G., 2004, A&A, 413, 1183
- [25] Rutten, R. J., de Wijn, A. G., Sütterlin, P., 2004, A&A, 416, 333
- [26] Sanchez Almeida, J., 2001, ApJ, 556, 928
- [27] Sanchez Almeida, J., Mrquez, I., Bonet, J. A., Domnguez Cerdea, I., Muller, R.. 2004, 609L, 91
- [28] Schmidt, H. U., Simon, G. W., Weiss, N. O., 1985, A&A, 148, 191
- [29] Solanki, S. K., Zufferey, D., Lin, H., Rueedi, I., Kuhn, J. R., 1996, A&A, 310L, 33
- [30] Spruit, H. C., 1979, SoPh, 61,363
- [31] Spruit, H. C., Zweibel, E. G., 1979, SoPh, 62, 15
- [32] Spruit, H. C., Zwaan, C., 1981, SoPh, 70, 207
- [33] Spruit, H. C., 1983, IAUS, 102, 41
- [34] Sütterlin, P., 2001, A&A, 374L, 21
- [35] Takeuchi, A., 1999, ApJ, 522, 518
- [36] van Ballegooijen, A. A., Nisenson, P., 2002, AAS, 200, 3801
- [37] Venkatakrisnan, P., 1985, JApA, 6, 21
- [38] Webb, A. R., Roberts, B., 1978, SoPh, 59, 249
- [39] Zwaan, C., Brants, J. J., Cram, L. E., 1985, SoPh, 95, 3

A The theory of convective collapse of magnetic fluxtubes

This appendix is added to give an insight into the physics of the magnetic fluxtubes that move through the atmosphere of the sun and that are observable as BPs in the photosphere and chromosphere.

Observations of the small-scale magnetic field in the atmosphere of the Sun show high field strengths, i.e. a magnetic flux density in the order of 500–2000 G (1 G = 1×10^{-4} Tesla). Parker (1978) suggested that these strengths are due to a convective process in an originally weaker field. He showed that a downward flow in a fluxtube can be maintained by buoyancy forces and that it is cooler than its surroundings. The result is that this temperature reduction causes a reduced pressure at the surface, which results in a high magnetic field.

Spruit and Zweibel (1979) determined that this process can only occur if the initial field strength is low enough, since a vertical magnetic field has a stabilizing effect on convection. The magnetic fluxtube (Fig. 26) becomes convectively unstable if the field strength is lower than the critical field strength derived by Spruit and Zweibel (1979). They find a critical field strength of $B_c = 1270$ G for the solar convection zone if the initial fluxtube was in temperature equilibrium with its surroundings. Their conclusion is that observed fluxtubes with higher field strengths are probably stable.

Spruit (1978) studied what happens if the tube becomes unstable. If the instability sets in as a downward flow, the tube cools with respect to its surroundings and its field strength increases, the higher field, however, has a stabilizing influence. Hence (Spruit and Zweibel, 1979), there is a limit to the downward displacement, i.e. the tube can transform into a new equilibrium state with a lower energy, lower temperature and higher field strength. On the other hand, if the instability sets in as an upward flow, the field strength decreases and the instability becomes stronger. One expects normal convection in a dispersed field to be the end result.

Hasan (1983) shows similar results in his modeling of the convective collapse of magnetic fluxtubes. Venkatakrishnan (1985) includes radiative heat transport in his model and concludes that heat transport reduces the efficiency of concentration of magnetic fields by convective collapse in the case of polytropic tubes.

Another important aspect of the magnetic fluxtubes is their three dimensional behaviour in granules and super-granules (Schmidt et al. 1985). Most of the magnetic flux is confined to isolated fluxtubes, whose motion is largely affected by the competing effects of magnetic buoyancy and granular or super-granular convection. It is well-accepted that these magnetic elements migrate towards the boundaries of the super-granules and congregate in the network (NW, Fig. 7). This effect of migration of flux is called flux expulsion. If their flux is less than $F_c \approx 10^{18}$ Mx (1 G = 1 Mx cm⁻²), they are observed between the granules in regions with downward velocity, the intergranular lanes, and are called small-scale magnetic elements. If $F_c > 10^{18}$ Mx the tubes no longer move towards the intergranular lanes.

Takeuchi (1999) uses Newton's law of cooling to take radiative energy transport into account. He finds the possibility of shock formation in his parameter space and the results show that shocks suppress the field amplification by con-

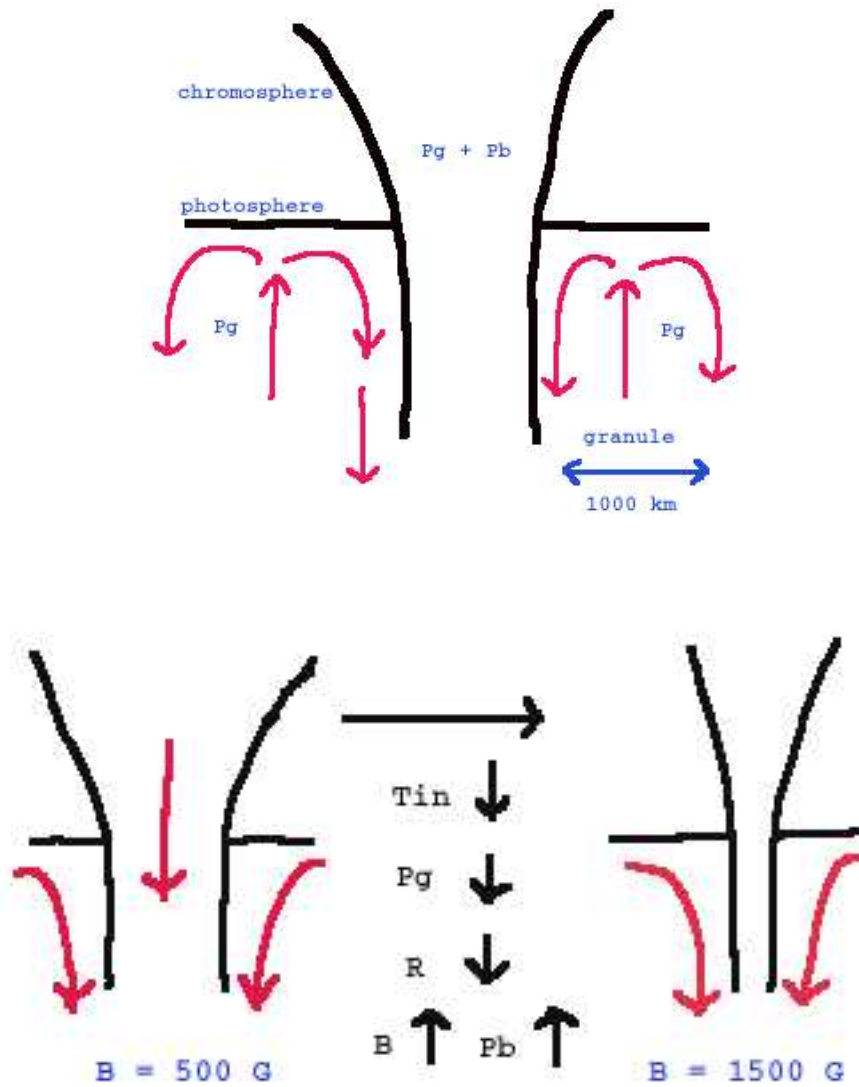


Figure 26: top: schematic view of a small-scale magnetic field concentration located between 2 granules extending from the convection zone into the chromosphere. P_g represents the gas pressure and P_b represents the magnetic pressure. Bottom: Schematic view of convective collapse, the tube becomes unstable and the gas starts to flow down. The temperature and pressure within the tube decreases, so the radius of the tube decreases as well. The result is a magnified magnetic field strength. T_{in} is the temperature inside the tube, R the radius and B the magnetic field strength.

vective collapse. He argues that all actually observed photospheric BPs are convectively stable.